The FASEB Journal

RESEARCH ARTICLE OPEN ACCESS

Mitigation of Ferroptosis in Diabetic Kidney Disease Through Mesenchymal Stem Cell Intervention via the Smad2/3/METTL3/S1PR1 Axis

Li-Lan Huang | Yue-Yuan Hou | Ji Yang | Xing-Na Liao | Jin-Sha Ma | Wen-Chao Wang | Yi-Xiao Quan | Hong-Ying Jiang | Yi-Hua Bai

Department of Nephrology, The Second Hospital Affiliated to Kunming Medical University, Kunming, China

Correspondence: Hong-Ying Jiang (1627248965@qq.com) | Yi-Hua Bai (baiyihua@kmmu.edu.cn)

Received: 12 December 2024 | **Revised:** 20 May 2025 | **Accepted:** 29 May 2025

Funding: Yunnan Revitalization Talent Support Program (Youth talent project [No. YNWR-QNBJ-2020-269]) and (Famous doctors project [No. YNWR-MY-2019-075]). Reserve Talents Project for Young and Middle-aged Academic and Technical Leaders in Yunnan Province (202005AC160024). Yunnan Fundamental Research Kunming Medical University Joint Projects (No. 202201AY070001-101). Kunming Medical University Innovation Fund for Postgraduates in 2024 (2024S271). The Second Affiliated Hospital of Kunming Medical University Talent Echelon Cultivation Project-Academic Leader (RCTDXS-202303). National Clinical Research Center of Chronic Kidney Disease, the Second Affiliated Hospital of Kunming Medical University (project No. GF2020003).

Keywords: diabetic kidney disease | ferroptosis | human umbilical cord mesenchymal stem cells | METTL3 | *S1PR1* | Smads

ABSTRACT

Diabetic kidney disease (DKD) is a leading cause of end-stage renal disease (ESRD) and is associated with heightened cardiovascular risk and increased overall mortality. Although mesenchymal stem cells (MSCs) have demonstrated therapeutic potential in DKD, their precise mechanisms of action have not been fully elucidated. This study aimed to investigate the involvement of Smad signaling, N6-methyladenosine (m6A) modifications, and ferroptosis in MSC-mediated treatment of DKD. Cellular and animal models of DKD were used to evaluate MSC intervention effects, supported by gene knockdown and overexpression experiments. Protein expression and phosphorylation levels of Smad2/3, m6A-associated enzymes, and markers of ferroptosis were assessed. Additionally, transcriptional targets associated with ferroptosis were identified through integrated transcriptome and m6A methylation sequencing analyses, followed by subsequent validation. Elevated Smad2/3 phosphorylation and ferroptosis were observed in DKD, while MSC interventions effectively alleviated these processes, resulting in improved renal lesions. Furthermore, MSC treatment reduced the heightened levels of m6A modification observed in DKD. Mechanistic investigations identified methyltransferase-like 3 (METTL3) as a key regulator of m6A modification in DKD. Suppression of METTL3 reversed the upregulated m6A modification and ferroptosis induced by Smad2 overexpression. Importantly, sphingosine-1-phosphate receptor 1 (*S1PR1*) was identified as a protective target gene against ferroptosis in DKD. In DKD models, Smad2 facilitated the m6A modification of the *S1PR1* gene by interacting with METTL3 following its nuclear translocation, thereby influencing S1PR1 expression and promoting cellular ferroptosis. Intervention with MSCs

Abbreviations: ALKBH5, AlkB homolog 5; ASCL4, Acyl-CoA synthetase long-chain family member 4; AUC, area under curve; CTGF, connective tissue growth factor; DKD, diabetic kidney disease; ELISA, enzyme-linked immunosorbent assay; EMT, epithelial-mesenchymal transition; ESRD, end-stage renal disease; FoxO, forkhead box O; FTO, fat mass and obesity-associated protein; GPX4, glutathione peroxidase 4; HGF, hepatocyte growth factor; HK-2, human kidney-2; IDO, indoleamine 2,3-dioxygenase; IF, immunofluorescence; IGF-1, insulin-like growth factor-1; IHC, immunohistochemistry; IL-10, interleukin-10; LDL, low-density lipoprotein; m6A, N6-methyladenosine; MeRIP-qPCR, methylated RNA immunoprecipitation-quantitative polymerase chain reaction; METTL14, methyltransferase-like 14; METTL3, methyltransferase-like 3; MPC5, mouse podocyte cell line 5; MSCs, mesenchymal stem cells; QPCR, quantitative polymerase chain reaction; S1P, sphingosine-1-phosphate; S1PR1, sphingosine-1-phosphate receptor 1; SLC3A2, solute carrier family 3 member A2; SLC7A11, solute carrier family 7 member 11; Smad, Smad family member; TGF-β1, transforming growth factor-beta 1; Th17, T helper 17 cell; WB, western blot; WTAP, Wilms' tumor 1-associating protein.

This is an open access article under the terms of the Creative Commons Attribution-NonCommercial-NoDerivs License, which permits use and distribution in any medium, provided the original work is properly cited, the use is non-commercial and no modifications or adaptations are made.

© 2025 The Author(s). *The FASEB Journal* published by Wiley Periodicals LLC on behalf of Federation of American Societies for Experimental Biology.

mitigated this process, providing further insights into the regulatory mechanisms through which MSCs modulate ferroptosis in podocytes affected by DKD.

1 | Introduction

Diabetic kidney disease (DKD), a prevalent microvascular complication of diabetes, has emerged as a significant cause of end-stage renal disease (ESRD) [1]. Recent findings highlight the critical role of podocyte loss in the progression of DKD [2–4]. As podocytes are non-regenerative and play a key role in maintaining the glomerular filtration barrier, strategies to protect and delay podocyte injury have become crucial to the management of DKD [5]. However, current clinical interventions for DKD often yield limited therapeutic outcomes, underscoring the urgent need for new treatment approaches [6, 7]. Mesenchymal stem cells (MSCs), recognized for their multipotency, low immunogenicity, and immunomodulatory properties, have indicated promise in alleviating DKD through various mechanisms [8–10]. Further investigation into the signaling pathways linking MSCs and DKD is essential to advance their clinical applications.

DKD leads to ferroptosis primarily due to oxidative stress induced by hyperglycemia. The free radicals generated by oxidative stress damage cell membranes and mitochondria, resulting in the release and accumulation of iron. This triggers ferroptosis, an iron-dependent form of programmed cell death, accompanied by lipid peroxidation, which ultimately exacerbates kidney cell damage and dysfunction [11]. Previous sequencing analyses of renal tubular epithelial cells (HK-2) identified an association between ferroptosis and DKD progression. Subsequent in vitro and in vivo studies confirmed that MSCs mitigate ferroptosis in HK-2 cells. Beyond HK-2 cells, ferroptosis contributes to podocyte loss, exacerbating DKD progression [12]. The underlying mechanisms may involve ubiquitination and lipid peroxidation, among other pathways [13]. However, the potential of MSCs to inhibit ferroptosis in podocytes remains unclear, warranting further investigation into this mechanism.

Smad2/3 are well-established downstream components of the Transforming Growth Factor-Beta 1 (TGF-β1) signaling pathway [14]. The TGF-β1/Smad axis is widely acknowledged as a pivotal mechanism underlying renal fibrosis in DKD [15]. Previous studies have demonstrated that intravenous administration of MSCs via the tail vein in DKD rat models suppresses Smad2/3 phosphorylation, thereby mitigating the progression of renal fibrosis and associated inflammation [16, 17]. Additionally, activation of the TGF-β1/Smad pathway in DKD has been linked to podocyte loss [18, 19].

In human embryonic stem cells (hESCs) and human induced pluripotent stem cells (hiPSCs), Smad2/3 has been revealed to interact with the METTL3-METTL14-WTAP complex, facilitating the m6A methylation of downstream signaling molecules [20]. m6A is the most prevalent reversible epigenetic modification on mRNA and influences biological processes by regulating mRNA stability [21, 22]. There is growing evidence that m6A modifications play a role in inflammatory responses and ferroptosis, both of which are critical pathogenic mechanisms in DKD [23, 24]. However, the potential interaction between Smad2/3 and methyltransferases in promoting disease progression in DKD podocytes remains to be elucidated.

This study investigated the roles of Smad2/3 signaling, methyltransferases, and ferroptosis in the pathogenesis of DKD. Findings identified sphingosine-1-phosphate receptor 1 (*S1PR1*) as a differentially methylated gene associated with m6A methylation, elucidating the mechanisms by which ferroptosis contributes to DKD progression. Additionally, the study highlights the therapeutic potential of MSCs in this context, providing a theoretical foundation for their application in DKD treatment.

2 | Materials and Methods

2.1 | Mouse Models

Mouse Models Male db/db and C57 mice, aged 8 weeks, were obtained from Hunan Sileike Jingda Laboratory Animal Co. Ltd. All animals were maintained under standard environmental conditions, including a controlled temperature of 21°C ± 2°C, humidity levels of 30% to 70%, and a 12-h light/dark cycle. Ethical compliance was ensured, and the study protocol received approval from the Animal Ethics Committee of the Second Affiliated Hospital of Kunming Medical University, Yunnan, China (Ethics No.: Kmmu20211132). The human umbilical cord-derived MSCs utilized in this experiment were purchased from Cyagen Biosciences Inc. (Guangzhou, China).

Following a one-week acclimatization period, C57 mice were assigned to the normal control group (Control group), while db/db mice were used to establish the DKD model. The DKD model was considered successfully established when random blood glucose levels reached or exceeded 16.7 mmol/L for three consecutive days [25]. The model mice were then randomly allocated into four groups ($n = 6$ per group) and subjected to the following interventions:

- Control Group: Normal conditions with the administration of an equal volume of physiological saline via tail vein injection.
- DKD Group: Physiological saline administered via tail vein injection following DKD model establishment.
- DKD + sh-NC Group: rAAV-NC (3×10^8 particles/mouse) injected via the tail vein every 4 weeks after DKD model establishment.
- DKD + sh-RNA Group: rAAV-X (3×10^8 particles/mouse) injected via the tail vein every 4 weeks following DKD model establishment.
- DKD + MSCs Group: MSCs administered via the tail vein at a dose of 1×10^6 cells/0.2 mL per mouse, given once per week after DKD model establishment.

After 8 weeks of interventions, samples were collected from the experimental animals for subsequent analysis.

2.2 | Cell Culture and Treatment

Plasmids encoding sh-Smad2, sh-METTL3, OE-Smad2, empty viral plasmids, and si-S1PR1 were obtained from HonorGene. Two microliters of each plasmid were introduced into 100 μL of competent *Escherichia coli* cells. Following transformation, a single colony was selected and cultured in 20 mL of liquid medium, incubated overnight at 37°C with shaking at 200 rpm. Plasmids were subsequently extracted and screened using Quantitative Polymerase Chain Reaction (qPCR) to identify optimal interference vectors. These vectors were then transfected into 293T cells for viral packaging.

Approximately 18 to 24 h prior to lentivirus infection, the culture medium was replaced with 2 mL of fresh medium containing 10 μg/mL polybrene. Virus suspensions or si-RNA were added, and incubation was carried out at 37°C for 8 h. The virus-containing medium was then replaced with fresh medium. Mouse podocyte cells (MPC5) were transfected with the prepared lentiviruses, and stable cell lines were selected using 2.5 μg/mL puromycin over a one-month period. Validation of the stable cell lines was conducted using qPCR and western blot (WB).

Cells were cultured in medium supplemented with 10% fetal bovine serum. This study used a Transwell system for co-culturing MPC5 cells and MSCs. In the experiment, MPC5 cells were treated with 25 μmol/L glucose in the culture medium for 72 h. After treatment, the MPC5 cells were co-cultured with MSCs at a 1:1 ratio for 72 h. The Transwell system separated the two cell types into different chambers, allowing indirect interaction through the culture medium. The cell number for each group was 1×10^5, ensuring consistent experimental conditions to investigate the interaction between MPC5 cells and MSCs under high-glucose conditions.

2.3 | CCK8 Assay

The cytotoxic effects of glucose on cells in vitro were assessed using a CCK8 assay. MSCs were seeded into 96-well plates at a density of 100 μL per well in low-glucose DMEM medium supplemented with 10% fetal bovine serum (FBS) and incubated at 37°C with 5% CO_2 for 24 h to allow cell adhesion. Notably, even in the 0 μmol/L glucose group, the basal medium and FBS may provide alternative energy sources such as amino acids and free fatty acids, which could support cell survival and proliferation.

Following adherence, the cells were treated with glucose at final concentrations of 0, 5, 15, 25, and 30 μmol/L. Subsequently, 10 μL of CCK8 solution was added to each well, and the plates were incubated at 37°C for 2–4 h. Optical density (OD) values were measured at 450 nm at time points of 0, 24, 48, 72, and 96 h to assess cell viability and proliferation.

2.4 | Flow Cytometry Analysis

Cells were washed with PBS, digested using trypsin, and subjected to centrifugation. The resulting cell pellet was fixed in 75% ethanol. After ethanol removal by centrifugation, the cells were resuspended in PBS buffer and stained with the appropriate working dye solutions. Staining included antibodies specific to Annexin V-PE/7-AAD, CD34, CD45, CD29, CD90, and reactive oxygen species (ROS).

Flow cytometry analysis was conducted using a BD FACSCalibur flow cytometer.

2.5 | Western Blot

Cells were lysed in 500 μL of RIPA lysis buffer (Servicebio) supplemented with protease inhibitors. Protein concentrations were determined using the BCA Protein Assay Kit (Beyotime). Proteins extracted from tissues were separated via 10% SDS-PAGE and transferred onto PVDF membranes (Millipore).

The membranes were blocked with 5% BSA (Solarbio) to prevent nonspecific binding.

After blocking, the membrane was incubated with the following primary antibodies: p-Smad2 (Affinity, 1:1000), Smad2 (Affinity, 1:3000), p-Smad3 (Affinity, 1:1000), Smad3 (Affinity, 1:1000), ALKBH5 (Affinity, 1:3000), FTO (Proteintech, 1:2000), KIAA1429 (LB, 1:1000), METTL3 (Proteintech, 1:1000), METTL14 (Proteintech, 1:3000), WTAP (Affinity, 1:1000), S1pr1 (abcam, 1:1000), β-actin (Proteintech, 1:25000). The membrane was then incubated with the secondary antibodies: HRP-conjugated goat anti-rabbit IgG (Servicebio, 1:3000) and HRP-conjugated goat anti-mouse IgG (Servicebio, 1:5000). Protein bands were detected using the enhanced chemiluminescence (ECL) detection kit (Affinity), and images were captured using the V-OPT imaging system. Band intensity analysis was performed using ImageJ software.

2.6 | Quantitative Polymerase Chain Reaction (qPCR)

RNA was extracted using TRIzol and assessed for quality and concentration using a NanoDrop ND-100 spectrophotometer. cDNA synthesis was conducted using the SureScript First-Strand cDNA Synthesis Kit under the following conditions: 25°C for 5 min, 50°C for 15 min, 85°C for 5 s, and held at 4°C.

The synthesized cDNA was diluted fivefold, and quantitative PCR was conducted using 5× BlazeTaq qPCR Mix with specific primer pairs targeting the factors of interest. Amplification was conducted over 40 cycles, with fluorescence signals measured to determine CT values. Relative expression levels were calculated using the $2^{-\Delta\Delta Ct}$ method.

2.7 | Immunofluorescence (IF) Experiment

Cells were fixed with 4% paraformaldehyde (PFA) for 30 min, followed by blocking for 1 h in PBS containing 2% Triton X-100 (PBST) and 5% goat serum to reduce nonspecific binding. Primary antibodies targeting Smad3 (Affinity, 1:100) and Smad2 (Huabio, 1:100) were applied and incubated overnight at 4°C.

After washing, cells were incubated with the corresponding secondary antibody, Alexa Fluor 488-conjugated goat anti-rabbit IgG (Servicebio, 1:500), for 1 h at 37°C. Fluorescent images were captured and analyzed using a fluorescence microscope.

2.8 | m6A Methylation Level Detection

The m6A modification level in total RNA was measured using the EpiQuik m6A RNA Methylation Quantification Kit (Colorimetric, EpigenTek). Following the protocol provided by the kit, absorbance readings were taken at 450 nm using a colorimetric assay. The m6A levels were quantified by referencing a standard curve generated during the procedure.

2.9 | Dot Blot

RNA was extracted using TRIzol, and the samples were spotted onto nylon membranes. The membranes were crosslinked using a UV crosslinker at 1200 mJ/cm^2 for 3 min. Following crosslinking, the membranes were washed with PBS containing 0.6% Tween-20 for 5 min and subsequently blocked with 5% skim milk for 1 h to prevent nonspecific binding.

The membranes were incubated overnight at 4°C with an m6A antibody (Abclonal, 1:1000). After three washes with TBST (10 min each), HRP-conjugated secondary antibodies, including HRP-conjugated goat anti-rabbit IgG (Invitrogen, 1:2500) and HRP-conjugated goat anti-mouse IgG (Servicebio, 1:5000), were applied and incubated for 30 min at room temperature. The membranes were then washed three times with TBST (10 min each) to complete the hybridization process with the m6A-specific monoclonal antibody.

Signal detection was conducted using an ECL chemiluminescent substrate, and images were captured using a gel imaging system.

2.10 | ELISA Assay

Reagents, samples, and standards were prepared in accordance with the instructions provided with the respective ELISA kits: the Ferrous Ion Content Kit (Ferrozine Method, Shanghai Jingkang), the IL-6 ELISA Kit, and the TNF-α ELISA Kit. Samples and enzyme conjugates were added to the wells, followed by incubation and subsequent washing steps as specified in the protocols.

Detection reagents were then applied, and chromogenic substrates were added to facilitate color development. The reactions were terminated using a stop solution, and absorbance was measured at 450 nm using a microplate reader (ELx800).

2.11 | Immunohistochemistry (IHC) Staining

Kidney tissues were fixed overnight in 4% paraformaldehyde (Guangfu), and subsequently dehydrated using a graded ethanol series (Chengdu Kelong). The tissues were then embedded in paraffin and sectioned into 5 μm slices for immunohistochemical analysis.

The sections were incubated with primary antibodies targeting Smad2 and Smad3. An enhanced enzyme-labeled polymer of goat anti-mouse/rabbit IgG was subsequently applied, and the sections were incubated at 37°C for 20 min. Staining was performed using DAB (Sapphire) and sections were counterstained with hematoxylin (Sapphire). After differentiation and bluing, the sections were dehydrated and mounted with neutral gum (Sapphire) for microscopic observation.

2.12 | Hematoxylin and Eosin (HE) Staining

Paraffin-embedded kidney tissue sections were cut into 5 μm thick slices using a microtome. The sections were stained with Mayer's hematoxylin (Sapphire) for 5 min, followed by rinsing under running water. Differentiation was performed using 1% hydrochloric acid ethanol for 5 s, and the sections were rinsed again under running water to restore the blue coloration.

The sections were then stained with eosin (Solarbio) for 1 min, with subsequent rinsing under running water to achieve optimal staining. Finally, the sections were dehydrated and mounted for microscopic observation.

2.13 | Masson Trichrome Staining

Masson trichrome staining was carried out using a kit obtained from Beijing Solarbio Science & Technology Co. Ltd. Paraffin-embedded kidney tissue sections were sequentially treated with solutions A, B, C, D, E, and F from the staining kit, following the instructions provided by the manufacturer.

After staining, the sections were washed with an acetic acid aqueous solution to achieve differentiation. The tissues were then dehydrated using anhydrous ethanol (Chengdu Kelong Chemical Co. Ltd.), cleared with xylene (XiLong Scientific Co. Ltd.), mounted, and subsequently examined under a microscope.

2.14 | MeRIP-qPCR (Methylated RNA Immunoprecipitation-qPCR)

Total RNA was extracted and purified using a PolyA mRNA purification kit. For immunoprecipitation (IP), m6A and IgG antibodies were individually mixed with IP buffer and incubated with protein A/G magnetic beads for 1 h to facilitate antibody-bead binding.

The purified mRNA was then combined with the magnetic bead-antibody complexes in IP buffer supplemented with ribonuclease and protease inhibitors and incubated overnight at 4°C. After incubation, the RNA was eluted using elution buffer, followed by extraction and purification using phenol-chloroform. The m6A-enriched RNA was subsequently analyzed by qPCR.

2.15 | Integrated Analysis of m6A RNA Methylation Sequencing and Transcriptome Sequencing

Total RNA was extracted and quality controlled from cell samples belonging to the MPC5 group, MPC5sh_METTL3 group, and MPC5sh_METTL3_G group. The analysis involved a comprehensive workflow comprising several key steps:

Library construction and evaluation—Libraries were prepared and assessed for quality prior to sequencing. The sequencing process included sample sequencing and screening, reference sequence alignment, peak calling, and differential peak analysis. Transcriptome sequencing analysis was performed, along with correlation analysis between transcriptome and m6A-seq data.

Potential m6A methylation modification sites were predicted using the SRAMP tool. Gene expression levels and their correlations were analyzed through the GEPIA platform.

2.16 | Transmission Electron Microscopy Observation

Approximately 30 mg of frozen tissue blocks were ground in liquid nitrogen, and RIPA protein lysis buffer was added for cell lysis. Following centrifugation, the cell pellets were resuspended in electron microscopy fixative and incubated for 4 h. After a second centrifugation, the supernatant was discarded, and the pellets were resuspended in phosphate buffer (PB) and embedded in agarose.

The embedded samples were fixed with 1% osmium tetroxide at room temperature, protected from light. Dehydration was then conducted using a graded series of alcohol and acetone. The samples were infiltrated with an embedding medium, using mixtures of acetone and 812 embedding resin at ratios of 1:1 and 1:2, respectively, before embedding in pure 812 resin.

The resin-embedded samples were transferred to embedding molds and polymerized in an oven. Ultrathin sections of the resin blocks were prepared using an ultramicrotome, stained, and examined under a transmission electron microscope. Images were captured for subsequent analysis.

2.17 | Statistical Analysis

Statistical analysis was performed using Prism GraphPad version 10.1.2. Experimental data are presented as mean ± standard deviation (Mean ± SD). Comparisons between two groups were conducted using the t-test, while comparisons among multiple groups were analyzed using one-way analysis of variance (One-way ANOVA). When ANOVA indicated statistically significant differences ($p < 0.05$), Tukey's post hoc test was applied for pairwise comparisons to further determine differences between groups. A value of $p < 0.05$ was considered statistically significant.

3 | Results

3.1 | In Vivo Experiments Demonstrate That MSCs Can Alleviate DKD

To assess the therapeutic effects of MSCs on DKD, MSCs were administered via tail vein injection in a DKD mouse model (The schematic diagrams are illustrated in Figure 1A,B) (validation shown in Figure S1A–E), and the expression of related factors was monitored. Blood glucose levels were significantly elevated in the DKD mice (Figure 1C), while the kidney weight/body weight ratio was reduced compared to the control group (Figure 1D).

Histological analysis showed that in the Control group, the glomerular structure was normal, with no significant mesangial proliferation. Renal tubules were arranged regularly, and no inflammatory cell infiltration was observed. In the DKD group, glomeruli were markedly enlarged with evident mesangial proliferation. Some renal tubular epithelial cells exhibited swelling, narrowed lumens, and infiltration of inflammatory cells (Figure 1E). Additionally, the expression of pro-inflammatory cytokines IL-6 and TNF-α was significantly elevated (Figure 1F).

In mice treated with MSCs, blood glucose levels were reduced, and the kidney weight/body weight ratio showed improvement (Figure 1C,D). In the DKD + MSCs group, compared with the DKD group, glomerular morphology was improved, mesangial proliferation was reduced, renal tubular structure was more intact, and inflammatory response was alleviated (Figure 1E). Furthermore, MSCs treatment reduced the secretion of inflammatory factors in the DKD mice (Figure 1F).

WB and IHC analyses revealed that the phosphorylation levels of Smad2 and Smad3 were significantly elevated in the renal tissues of DKD mice compared to the control group. Following MSCs intervention, the phosphorylation levels of Smad2/3 were markedly reduced (Figure 1G,H).

Previous studies have shown that MSCs inhibit ferroptosis in HK-2 cells exposed to high glucose, thereby alleviating apoptosis and EMT (Figure S2A–C). Bioinformatics analyses identified ACSL4 and SLC3A2 as differentially expressed genes following MSCs treatment (Figure S2D,E), with both genes implicated in the regulation of ferroptosis [26–28]. In addition, literature has reported that ferroptosis can also exert pathogenic effects in podocytes [29]. To assess whether MSCs inhibit ferroptosis in DKD, WB analysis was performed to examine ferroptosis-related protein levels. Compared to the control group, the DKD group exhibited increased ACSL4 levels and decreased GPX4 and SLC7A11 levels. MSCs intervention reversed these changes, reducing ACSL4 levels while increasing GPX4 and SLC7A11 expression (Figure 1I), suggesting that MSCs may regulate the overall expression of ferroptosis-related proteins in renal tissue.

Overall, these findings indicate that MSCs alleviate inflammation, Smad pathway activation, and ferroptosis, thereby improving diabetic nephropathy in the DKD mouse model.

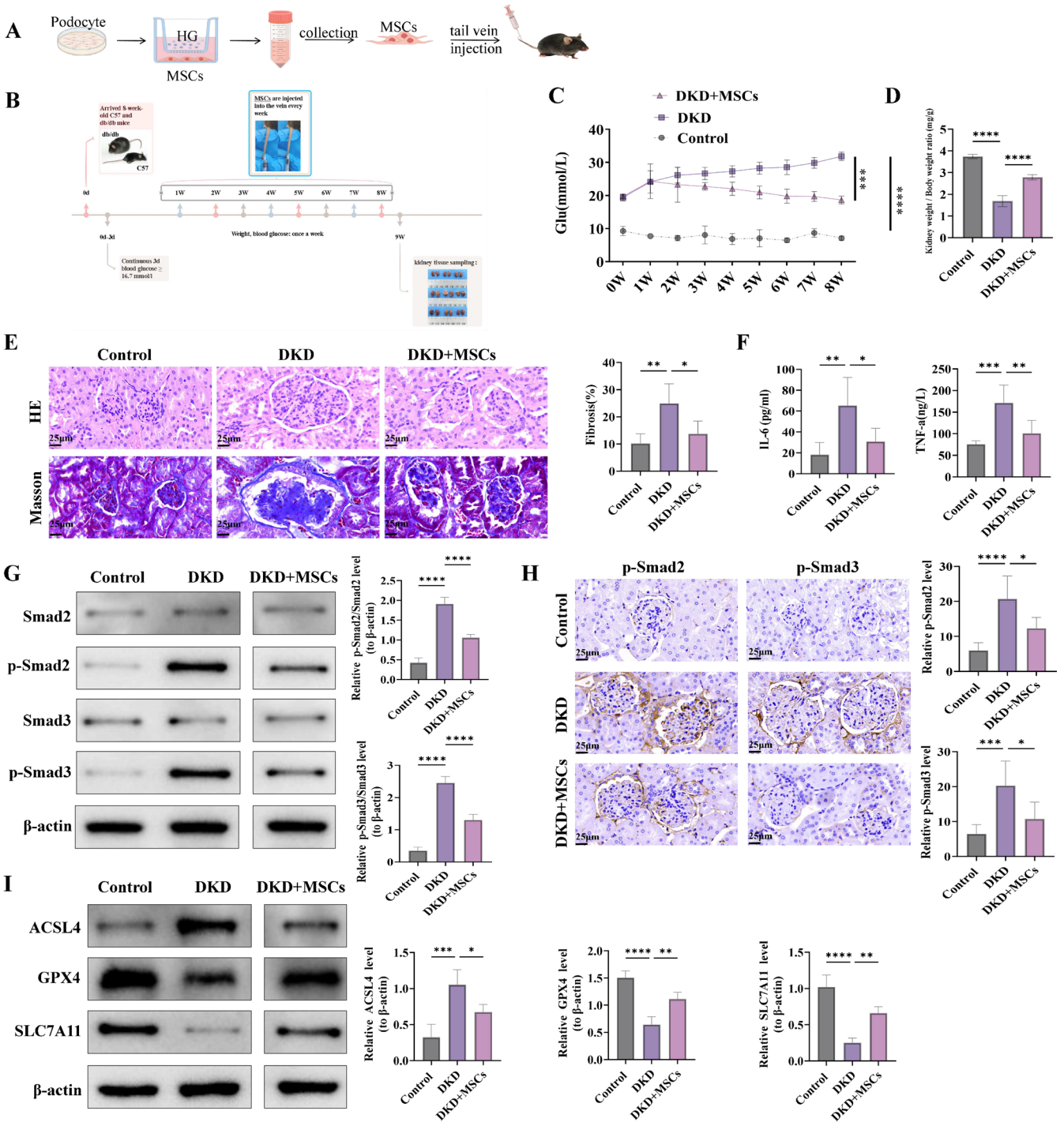

FIGURE 1 | Effects of MSC intervention on renal pathology, inflammation, Smad2/3 activation, and ferroptosis in DKD Mice: (A, B) Schematic representation of the modeling and intervention process in C57 and db/db mice. (C) Blood glucose levels monitored across the experimental groups. (D) Comparison of Kidney weight/Body weight ratios between groups. (E) H&E staining to assess renal pathological changes, and Masson staining to quantify renal fibrosis. Representative histopathological images are provided, with Masson staining quantification depicted on the right. (F) ELISA detection of IL-6 and TNF-α levels as markers of inflammation. (G) Western blot analysis of Smad2, Smad3, and their phosphorylated forms (p-Smad2, p-Smad3), with β-Actin as the loading control. (H) Immunohistochemistry to visualize p-Smad2/3 nuclear translocation, with magnification at 200× and nuclear staining shown in blue. (I) Western blot analysis of ferroptosis-related proteins (ACSL4, GPX4, and SLC7A11), using β-Actin as the loading control. Control Group: C57 Mice on a standard diet, administered an equal volume of physiological saline via tail vein injection. DKD Group: db/db mice with an established T2DM model, receiving physiological saline via tail vein injection. DKD + MSCs Group: db/db mice with an established T2DM model, treated with MSCs (1×10^6 cells/0.2 mL per mouse) via weekly tail vein infusion. Interventions were conducted over an 8-week period. Each group consisted of 6 mice, and all mice participated in and underwent all experimental assessments. All in vitro experiments were performed with at least three independent replicates (*$p < 0.05$; **$p < 0.01$; ***$p < 0.001$; ****$p < 0.0001$).

3.2 | MSCs Inhibit High-Glucose-Induced Injury in MPC5 Cells

The effects of MSCs on DKD were further validated through co-culture experiments with high-glucose-induced MPC5 cells (The schematic diagrams are illustrated in Figure 2A). The establishment of the high-glucose injury model in MPC5 cells is presented in Figure S1F,G. Co-culture of high-glucose-injured MPC5 cells with MSCs alleviated slowed cell growth and reduced apoptosis levels (Figure 2B,C). MSCs exert protective effects on podocytes through the secretion of cytokines or growth factors. Consequently, we employed ELISA to quantify the expression levels of these relevant factors. Compared to the control group, the high-glucose group (HG) exhibited decreased IL-10 and hepatocyte growth factor (HGF) levels and increased TGF-β, indoleamine-2,3-dioxygenase (IDO), and Insulin-like growth factor-1 (IGF-1) levels. Co-culture with MSCs reversed these changes, increasing IL-10 and HGF levels while reducing TGF-β, IDO, and IGF-1 expression (Figure 2D).

Transmission electron microscopy analysis demonstrated that MSC intervention improved mitochondrial morphological abnormalities in MPC5 cells caused by high-glucose exposure (Figure 2E).

Consistent with in vivo findings, MSCs reduced the phosphorylation of Smad2 and Smad3 induced by high glucose (Figure 3A,B).

IF analysis revealed increased nuclear translocation of Smad2 and Smad3 in the HG compared to the control group. Co-culture

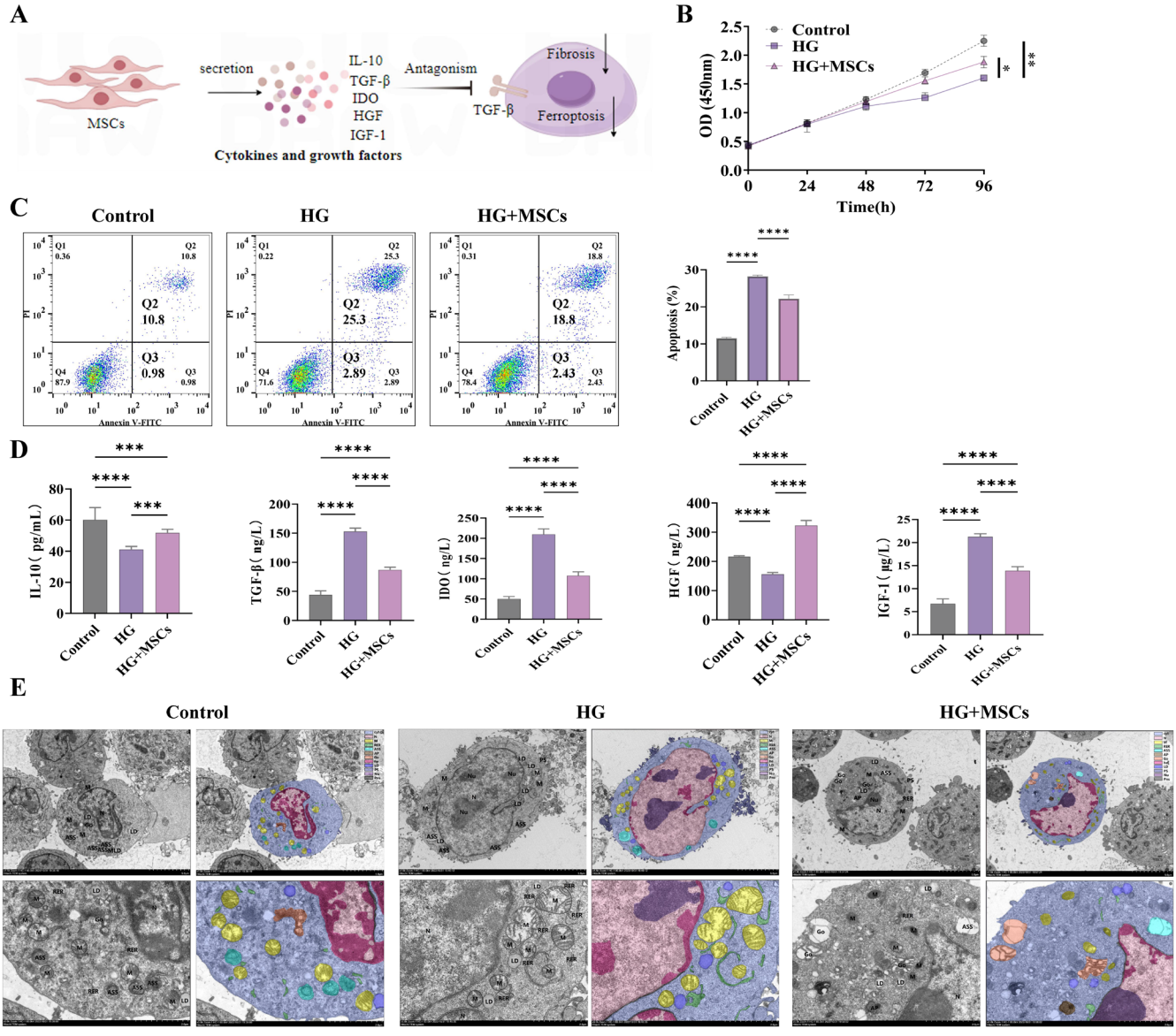

FIGURE 2 | MSCs inhibit high-glucose-induced injury in MPC5 cells: (A) Schematic diagram. (B) Cell proliferation assessed using a CCK8 assay. (C) Apoptosis rates analyzed via flow cytometry, with the corresponding bar chart quantification presented on the right. (D) ELISA detection of IL-10, TGF-β, IDO, HGF, and IGF-1 levels. (E) Transmission electron microscopy to observe morphological changes in MPC5 cells under high-glucose conditions and after co-culture with MSCs. Structural features are annotated as follows: PS (pseudopodia), cyt (cytoplasm), N (nucleus), M (mitochondria), RER (rough endoplasmic reticulum), LD (lipid droplet), and ASS (autophagic lysosome). All in vitro experiments were performed with at least three independent replicates (*$p < 0.05$; **$p < 0.01$; ***$p < 0.001$; ****$p < 0.0001$).

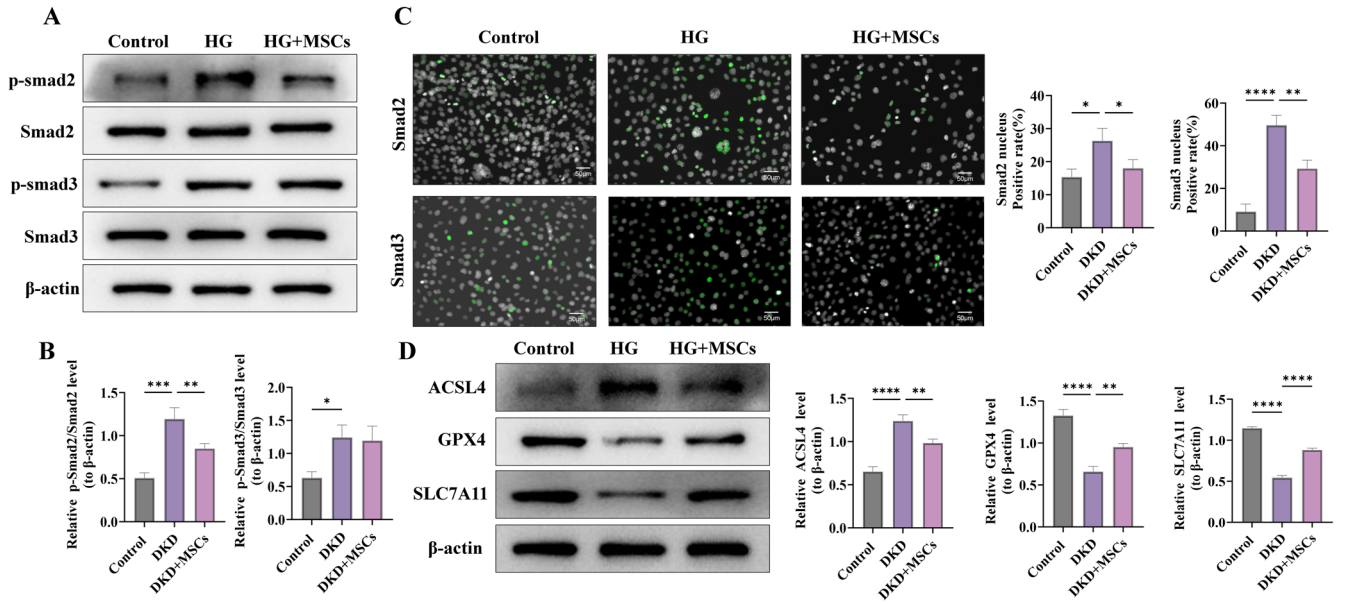

FIGURE 3 | MSCs inhibit the activation of the Smad2/3 pathway and ferroptosis. (A, B) Western blot analysis of Smad2, Smad3, and their phosphorylated forms (p-Smad2, p-Smad3), with β-Actin as the loading control. (C) Immunofluorescence analysis of Smad2/3 nuclear localization. Nuclei stained white, while Smad2/3 are labeled green using goat anti-rabbit IgG H&L (Alexa Fluor 488) secondary antibody. (D) Western blot analysis of ferroptosis-related proteins (ACSL4, GPX4, and SLC7A11), with β-Actin as the loading control. Grouping: Control Group: MPC5 Cells cultured in standard medium. HG Group: MPC5 Cells treated with 25 μmol/L glucose in standard medium for 72 h. HG + MSCs Group: MPC5 Cells co-cultured with MSCs in medium containing 25 μmol/L glucose for 72 h. All in vitro experiments were performed with at least three independent replicates (*$p < 0.05$; **$p < 0.01$; ***$p < 0.001$; ****$p < 0.0001$).

with MSCs significantly reduced the nuclear translocation of Smad2 and Smad3 in MPC5 cells (Figure 3C).

Additionally, WB analysis of ferroptosis-related proteins in the co-culture model revealed trends consistent with those observed in the animal experiments, including decreased ACSL4 levels and increased GPX4 and SLC7A11 expression following MSC intervention (Figure 3D).

These results collectively demonstrate that MSCs mitigate DKD-associated damage by inhibiting the activation of the Smad2/3 pathway and ferroptosis.

3.3 | MSCs Can Reduce m6A Modification in DKD Through METTL3

Previous studies have indicated that m6A modification plays a regulatory role in ferroptosis [30, 31]. To investigate this further, Dot blot analysis and the EpiQuik kit were used to assess m6A modification levels in DKD. The results demonstrated elevated m6A levels in high-glucose-induced MPC5 cells and the DKD animal model. Notably, MSC intervention effectively reduced these elevated levels (Figure 4A–D).

m6A modification is mediated by m6A-related enzymes. Previous studies have identified 28 genes associated with m6A modification through systematic analyses [32]. To further explore the involvement of m6A in DKD, we analyzed the publicly available microarray dataset GSE96804 from the GEO database, which was based on the GPL17586 platform and includes 20 normal control samples and 41 DKD samples. Expression data of 28 m6A-related genes were extracted from this dataset, and differential expression analysis was performed using the t-test. The results revealed significant differences in the expression levels of multiple m6A regulators between DKD and control samples, suggesting that m6A modification may be involved in the pathogenesis of DKD. These genes include CBLL1, METTL3, METTL5, WTAP, ALKBH5, FTO, ELAVL1, FMR1, HNRNPA1, HNRNPC, IGF2BP2, LRPPRC, RBMX, YTHDC2, and YTHDF2 (Figure 4E).

WB analysis further revealed specific changes in m6A enzyme expression. ALKBH5 and FTO were upregulated in the HG but were downregulated after co-culture with MSCs. Conversely, KIAA1429 and METTL3 exhibited the opposite expression trends (Figure 4F).

To further explore the diagnostic value of the methyltransferases METTL3, METTL14, and ALKBH5 in DKD, ROC curves for the three genes were generated using the pROC package. The results indicated that METTL3 and ALKBH5 exhibited excellent diagnostic performance, with AUC values greater than 0.8, while METTL14 showed poor diagnostic performance with an AUC of 0.591. METTL3 and ALKBH5 were significantly different between normal and disease groups, suggesting that these two m6A methyltransferases play important roles in DKD (Figure 4G).

These findings indicate that in DKD, MSCs can reduce the increase in m6A modification induced by elevated METTL3 levels, thereby influencing disease progression and potentially mitigating ferroptosis.

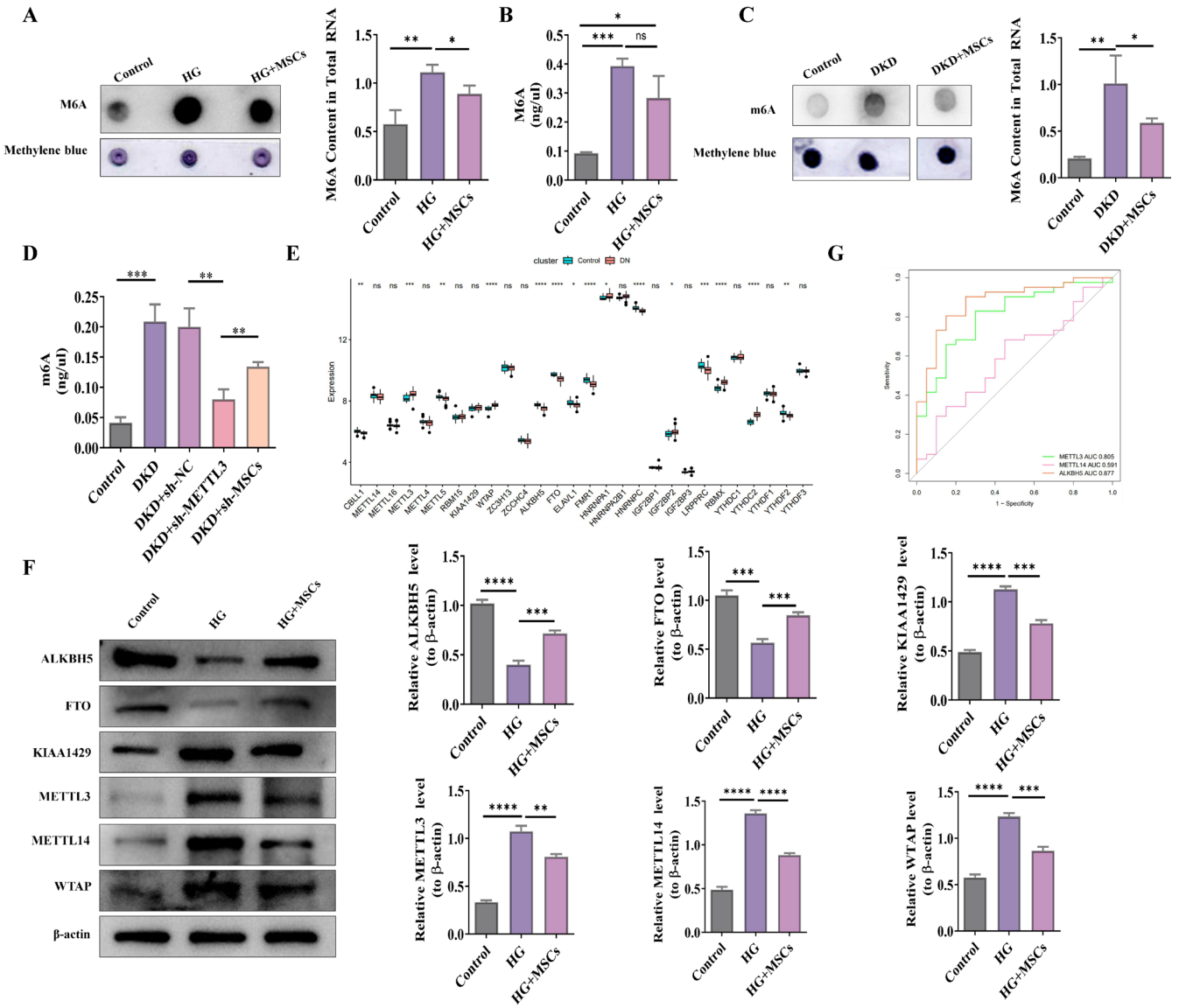

FIGURE 4 | MSCs reduce m6A modifications in DKD through METTL3: (A) Dot blot assay detecting m6A methylation levels in MPC5 cells, with methylene blue as a loading control. (B) Quantification of total m6A levels in RNA from MPC5 cells using the EpiQuik M6A RNA Methylation Quantification Kit. (C) Dot blot assay detecting m6A methylation levels in mouse kidney tissues, with methylene blue as a loading control. (D) Quantification of total m6A levels in RNA from mouse kidney tissues using the EpiQuik M6A RNA Methylation Quantification Kit. (E) Bioinformatics analysis of the expression of 21 methyltransferase enzymes in diabetic nephropathy, identifying key genes involved in m6A modifications. (F) Western blot analysis of protein levels of ALKBH5, FTO, KIAA1429, METTL3, METTL14, and WTAP, using β-Actin as the loading control. (G) ROC curve analysis assessing the diagnostic value of METTL3, METTL14, and ALKBH5. These analyses highlight the role of MSCs in reducing m6A modifications in DKD via modulation of METTL3 expression and activity. Each group consisted of 6 mice, and all mice participated in and underwent all experimental assessments. All in vitro experiments were performed with at least three independent replicates (*$p < 0.05$; **$p < 0.01$; ***$p < 0.001$; ****$p < 0.0001$).

3.4 | Knockdown of Smad2 Reduces m6A Modification and Ferroptosis

To investigate the relationship between increased METTL3 levels and Smad2/3 in DKD, a Smad2 knockdown cell line was established (Figure S3). The impact of Smad2 knockdown on m6A modification was assessed, revealing a significant reduction in cellular m6A levels following Smad2 knockdown (Figure 5A,B).

Since changes in m6A levels are often linked to changes in m6A-related enzymes, the effects of Smad2 on these enzymes were further examined. WB analysis indicated that Smad2 knockdown mitigated the high-glucose-induced increase in METTL3 and METTL14 expression, while at the same time reversing the decrease in ALKBH5 expression (Figure 5C).

Additionally, Flow cytometry was used to detect ROS levels and the percentage of ROS-positive cells. ELISA was used to measure the intracellular Fe^{2+} content, and WB was employed to assess the expression levels of ACSL4, GPX4, and SLC7A11 proteins. Smad2 knockdown reduces the levels of ROS, Fe^{2+}, and ACSL4, which are key markers of ferroptosis. Conversely, levels

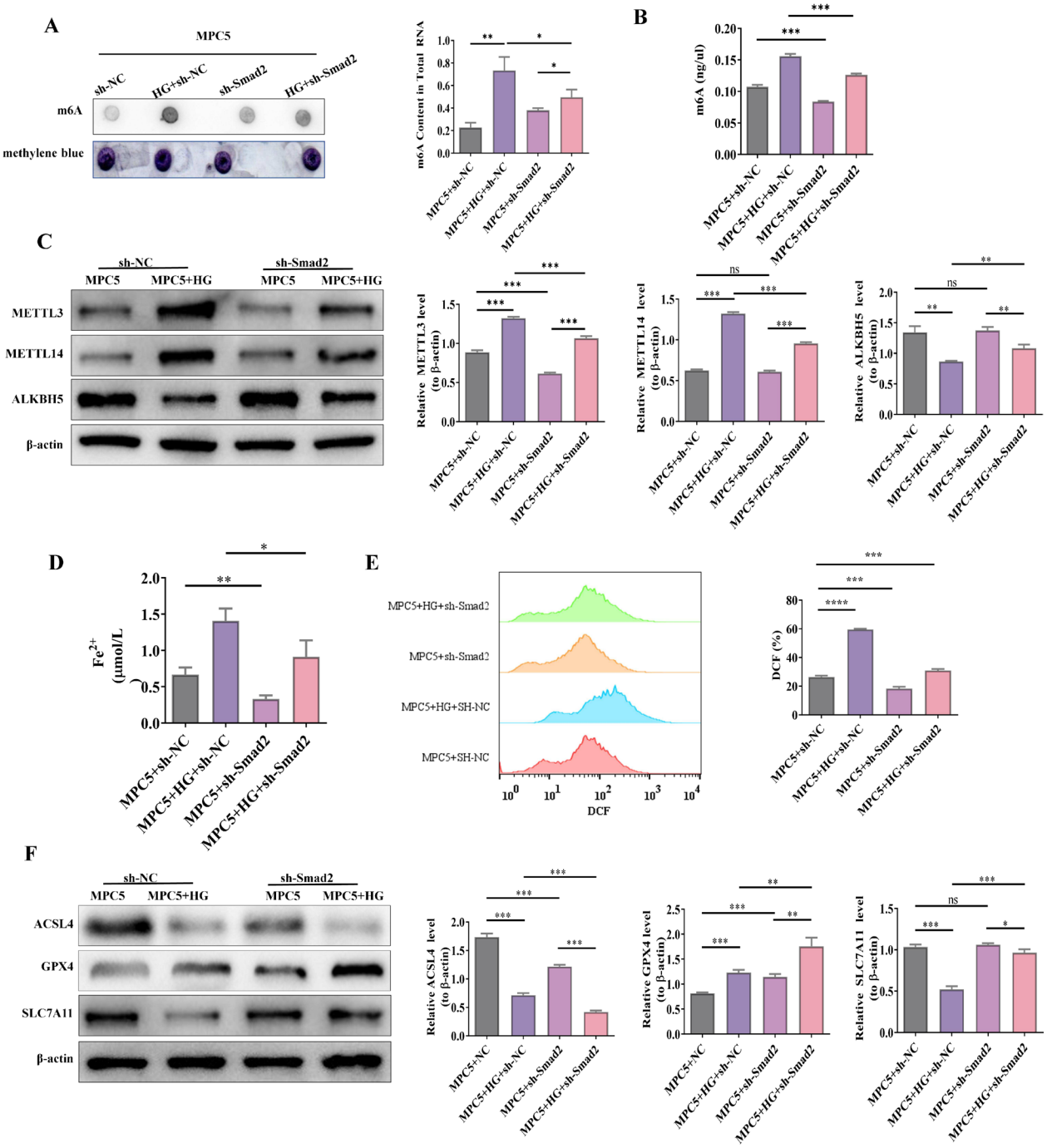

FIGURE 5 | In Vitro validation of the effects of sh-Smad2 on m6A modifications and ferroptosis: (A) Dot blot assay detecting m6A methylation levels in MPC5 cells, with methylene blue as the loading control. (B) Measurement of total m6A levels in RNA from MPC5 cells using the EpiQuik M6A RNA Methylation Quantification Kit. (C) Western blot analysis of ALKBH5, METTL3, and METTL14 protein levels, with β-actin as the loading control. (D) ELISA assay measuring Fe^{2+} content in MPC5 cells transfected with sh-Smad2. (E) Flow cytometry analysis of ROS levels in MPC5 cells transfected with sh-Smad2, with flow cytometry plots for ROS content and bar charts summarizing the results. (F) Western blot analysis of ferroptosis-related proteins ACSL4, GPX4, and SLC7A11 in MPC5 cells transfected with sh-Smad2, using β-actin as the loading control. All in vitro experiments were performed with at least three independent replicates (*$p < 0.05$; **$p < 0.01$; ***$p < 0.001$; ****$p < 0.0001$).

of GPX4 and SLC7A11, which are associated with ferroptosis inhibition, were increased (Figure 5D–F).

These findings collectively demonstrate that Smad2 knockdown reduces cellular m6A modification and ferroptosis, indicating a potential mechanistic link between Smad2, METTL3, and ferroptosis in DKD.

3.5 | Knockdown of METTL3 Can Alleviate the Effects of Ferroptosis

To confirm the role of METTL3 in regulating m6A modification, METTL3 was knocked down in both in vivo and in vitro models (Figure S4). In high-glucose-induced MPC5 cells, ferroptosis-related markers were detected in stable cell lines overexpressing

Smad2 and interfering with METTL3. Flow cytometry was used to detect ROS levels and the percentage of ROS-positive cells; ELISA was used to measure intracellular Fe^{2+} content. The results revealed that METTL3 knockdown significantly reduced m6A levels (Figure S5A,B). Furthermore, the knockdown of METTL3 reversed the elevated m6A modification levels induced by Smad2 overexpression (Figures S3 and S5C,D), indicating that Smad2 regulates m6A modification via METTL3.

In high-glucose-induced MPC5 cells, knockdown of METTL3 (sh-METTL3) inhibited ferroptosis, as evidenced by reduced levels of Fe^{2+} content, ROS, and ferroptosis markers (Figure 6A–D). These findings were corroborated in DKD mice with METTL3 knockdown. Mice exhibited increased body weight and kidney weight/body weight ratios, decreased blood glucose levels, and improved kidney gross specimen pathology (Figure 6E–H).

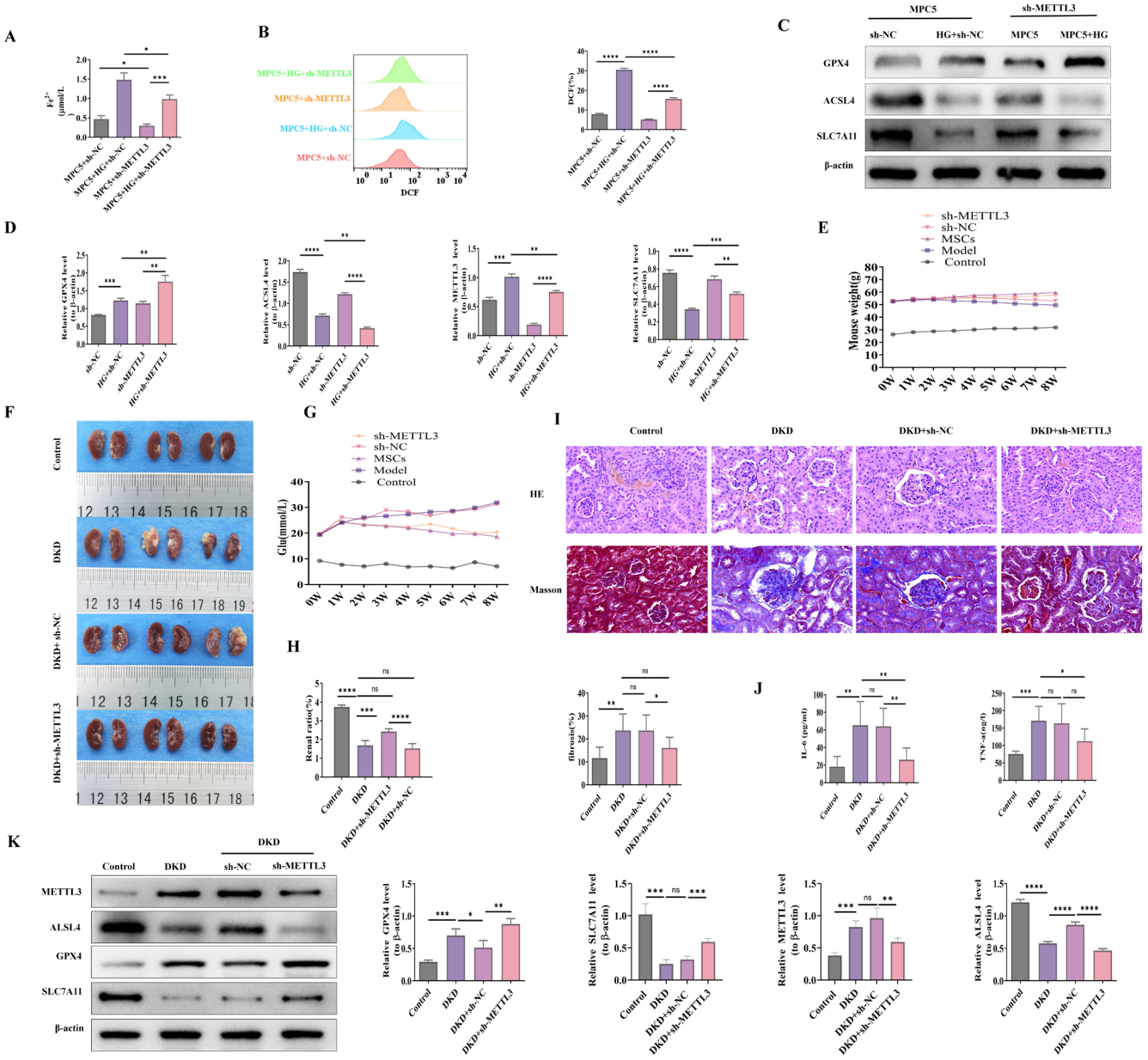

FIGURE 6 | Effects of sh-METTL3 on ferroptosis: (A) ELISA assay measuring Fe^{2+} content in MPC5 cells transfected with sh-METTL3. (B) Flow cytometry analysis of ROS levels in MPC5 cells transfected with sh-METTL3, showing flow cytometry plots and bar charts quantifying ROS content. (C) Western blot analysis of ferroptosis-related proteins ACSL4, GPX4, and SLC7A11 in MPC5 cells transfected with sh-METTL3, with β-actin as the loading control (band images). (D) Bar chart summarizing Western blot results for ACSL4, GPX4, and SLC7A11 protein expression levels in MPC5 cells transfected with sh-METTL3. (E) Measurement of mouse body weight across experimental groups. (F) Images of gross renal specimens. (G) Monitoring of blood glucose levels in experimental mice. (H) Kidney weight/Body weight ratio across groups. (I) Histological analysis of renal tissue using H&E and Masson staining to assess pathological changes and fibrosis. (J) ELISA assay measuring the expression levels of pro-inflammatory cytokines IL-6 and TNF-α in renal tissue. (K) Western blot analysis of METTL3, ACSL4, GPX4, and SLC7A11 protein levels in mouse kidney tissue, using β-actin as the loading control. Each group consisted of 6 mice, and all mice participated in and underwent all experimental assessments. All in vitro experiments were performed with at least three independent replicates (*$p < 0.05$; **$p < 0.01$; ***$p < 0.001$; ****$p < 0.0001$).

Histological analysis revealed that renal tissue damage and fibrosis were alleviated in DKD mice with METTL3 knockdown (Figure 6I). ELISA results indicated reduced expression of pro-inflammatory cytokines IL-6 and TNF-α (Figure 6J). Similar trends were observed in ferroptosis-related protein levels, with decreased ferroptosis markers in renal tissue (Figure 6K).

These results indicate that targeting METTL3 exerts a protective effect in DKD, primarily by reducing ferroptosis in podocytes. This highlights METTL3 as a key mediator of m6A modification and ferroptosis, with potential as a therapeutic target for DKD, primarily achieved through the reduction of ferroptosis in podocytes.

3.6 | RNA-Seq and m6A-Seq Correlation Analysis Reveals Target Gene as *S1PR1*

To identify downstream signaling molecules influenced by Smad2/3 and METTL3, RNA-seq and m6A-seq correlation analyses were conducted on cell samples from the MPC5 group, MPC5sh_METTL3 group, and MPC5sh_METTL3_G group (Figure 7A,B). Particular attention was given to peaks where m6A modification levels were reduced, while transcription levels were increased, highlighted by the blue section in the analysis (Figure 7C).

Gene Ontology (GO) and KEGG pathway analyses identified 43 differentially expressed genes enriched in non-canonical Wnt signaling pathways and nucleotide-binding functions, as well as 59 differentially expressed pathways, including the PI3K-Akt signaling pathway, mTOR signaling pathway, and Wnt signaling pathway (Figure 7D–F).

Among the differentially expressed genes linked to ferroptosis and meeting the research criteria (Tables S1 and S2), *S1PR1* emerged as the only candidate. Further analysis using the GEPIA database revealed a strong association between S1PR1, Smad2, and METTL3 (Figure 7G). Nine potential m6A modification sites on S1PR1 mRNA were predicted, with eight sites revealing a confidence level exceeding 95% using the SRAMP tool (Figure 7H).

We analyzed the potential binding proteins of S1PR1 and identified SLC7A11 as a potential binding partner for S1PR1.

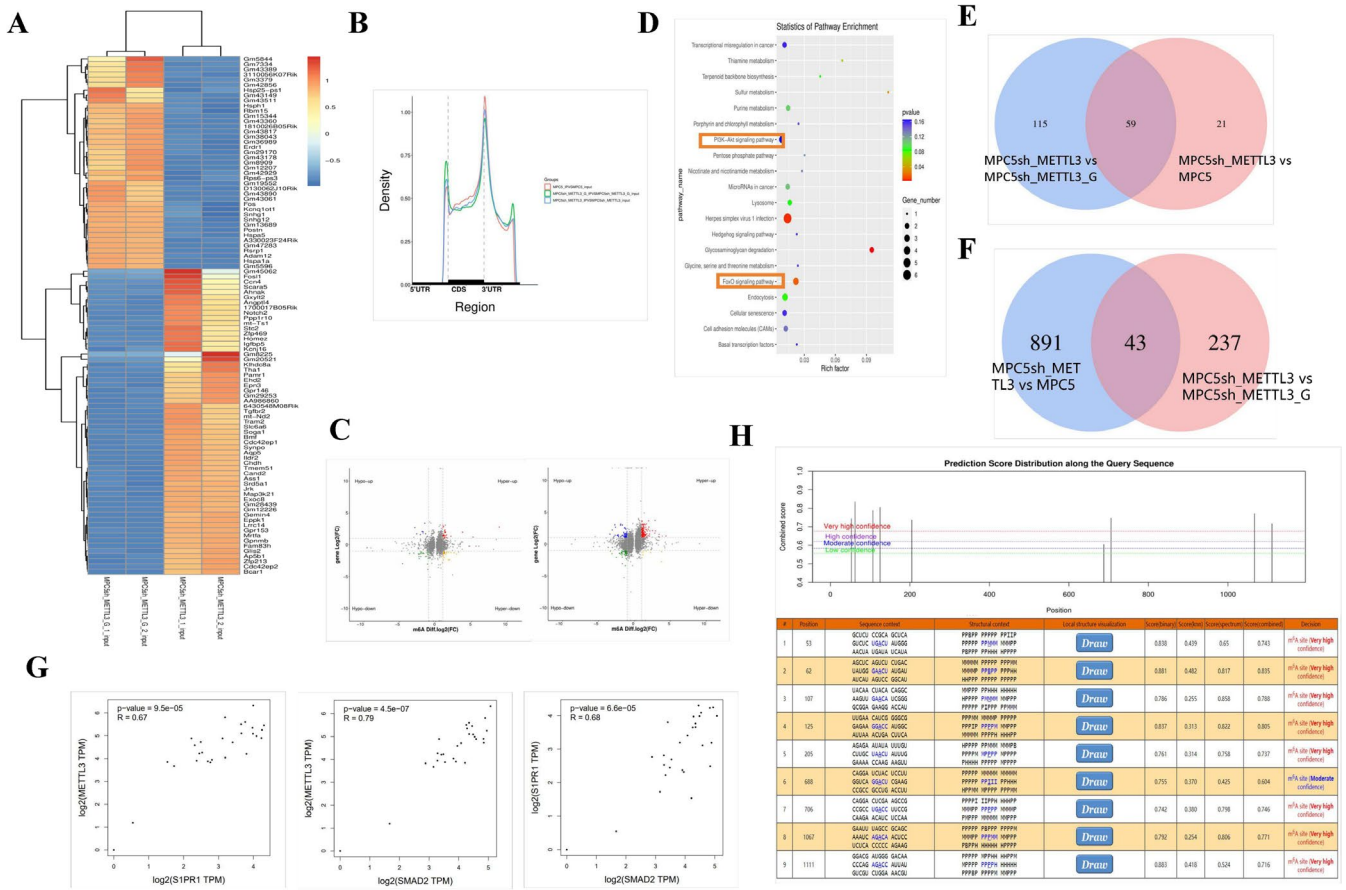

FIGURE 7 | Transcriptome sequencing to identify differentially expressed genes and pathways: (A) Heatmap depicting the clustering of differentially expressed genes. (B) Peak density curves representing the distribution of m6A peaks across the 5′ UTR, CDS, and 3′ UTR regions. (C) Quadrant plot comparing differentially expressed genes and differentially methylated m6A peaks. (D) KEGG enrichment analysis identifying pathways associated with significantly differentially expressed genes with m6A methylation. (E) Venn diagram highlighting overlaps in enriched KEGG pathways. (F) Venn diagram revealing overlaps in differentially expressed genes across experimental groups. (G) Correlation analysis of Smad2, METTL3, and *S1PR1* gene expression using the GEPIA database, with an R-value greater than 0.3 indicating a positive correlation. (H) Prediction of potential m6A methylation modification sites on S1PR1 mRNA using the SRAMP tool.

Molecular docking was employed to evaluate the binding affinities between S1PR1 and SLC7A11 proteins using the HDOCK tool. The results show that the docking scores are −481.85 kcal/mol (Figure 8A,B, Table S3). Co-IP assay further confirmed their binding (Figure 8C).

To investigate the molecular interactions between S1PR1 and the METTL3/Smad2 protein complex molecular docking was employed to evaluate the binding affinities of Smad2 with S1PR1-mRNA using the HDOCK tool. The results show that the docking scores for Smad2 with S1PR1-mRNA are −344.57 kcal/mol (Figure 8D,E, Table S4), denoting strong binding affinities. To determine whether METTL3 is able to bind to the promoter of S1PR1, a CHIP-PCR assay was performed. Our data demonstrated that METTL3 was able to bind to the promoter region of S1PR1 (Figure 8F). Finally, Co-IP assays demonstrated a protein–protein interaction between Smad2 and METTL3 (Figure 8G). These results indicate that the Smad2/3/METTL3 pathway may regulate ferroptosis by modulating both the m6A modification levels and transcriptional activity of S1PR1 mRNA (Figure 8H).

3.7 | METTL3 Promotes m6A Modification of S1PR1 and Reduces Its Expression, Regulating Cellular Ferroptosis

Based on sequencing analysis, *S1PR1* was identified as a downstream target gene. Expression levels of S1PR1 were analyzed under various conditions. qPCR results revealed that overexpression of Smad2 significantly reduced S1PR1 expression, while knockout of METTL3 restored S1PR1 expression levels (Figures S3 and S6A). WB analysis further confirmed that S1PR1 expression was significantly increased following knockdown of either Smad2 or METTL3 (Figure S6B). These findings indicate an inverse relationship between S1PR1 expression and Smad2/METTL3 levels.

MeRIP-qPCR analysis supported these observations. S1PR1 expression was higher in the anti-m6A group compared to the input group. In HG conditions, S1PR1 expression was reduced in the MPC5 + HG group when compared to the control MPC5 group. However, S1PR1 expression was increased in the MPC5 + HG + sh-METTL3 group or MPC5 + HG + sh-Smad2 group compared to the MPC5 + HG + sh-NC group (Figure S6C). These results confirm that METTL3/Smad2 regulates m6A modification of S1PR1, establishing it as a downstream target of Smad2/3 and METTL3.

To examine the role of S1PR1 in ferroptosis, an MPC5 cell line with simultaneous knockdown of S1PR1 and METTL3 was constructed (Figure S7). Flow cytometry was used to detect ROS levels and the percentage of ROS-positive cells; ELISA was used to measure intracellular Fe^{2+} content; and WB was employed to assess the expression levels of ACSL4, GPX4, and SLC7A11 proteins. When compared to the MPC5 + sh-METTL3 group, the knockdown of S1PR1 reversed the protective effects of METTL3 knockdown on ferroptosis in DKD (Figure 9A–D).

In DKD mouse kidney tissues, S1PR1 levels were reduced. However, S1PR1 expression was increased following MSC treatment or METTL3 knockdown (Figure 9E–H).

4 | Discussion

DKD is associated with an increased risk of cardiovascular disease and overall mortality [33]. The majority of patients with DKD have type 2 diabetes, as its prevalence far exceeds that of type 1 diabetes [34]. Consequently, a more comprehensive understanding of the pathogenic mechanisms underlying type 2 diabetic nephropathy is essential for advancing therapeutic approaches for the broader DKD population.

Recent preclinical studies have demonstrated that MSCs can mitigate the progression of DKD [35]. Among various MSC sources, including adipose tissue, bone marrow, and liver, human umbilical cord mesenchymal stem cells (UC-MSCs) present distinct advantages [36]. These cells are obtained through a non-invasive collection process, exhibit minimal immune rejection, and possess superior immunomodulatory properties, making them particularly promising for clinical application [37, 38]. UC-MSCs have been revealed to significantly improve renal function in preclinical studies [39, 40].

In this study, UC-MSCs were selected as the therapeutic cells for DKD. The findings demonstrated that UC-MSC administration improved blood glucose levels, reduced the release of pro-inflammatory cytokines, and alleviated kidney fibrosis and pathological changes in a DKD mouse model. In addition, we observed that the body weight of mice in the MSC-treated group showed improvement compared to the untreated DKD group, suggesting that MSC treatment could, to a certain extent, alleviate the weight loss induced by diabetes. These results further substantiate the therapeutic potential of UC-MSCs in the treatment of DKD.

Previous research has demonstrated that MSCs inhibit renal fibrosis by suppressing the activation of the TGF-β/Smad signaling pathway. For instance, in DN rat models, Masson's trichrome staining revealed significant interstitial fibrosis, which was mitigated by MSC treatment in DKD rats [16]. Further studies indicated that the administration of TGF-β1 weakened the protective effects of MSCs on renal injury in DN mice, accompanied by activation of Smad phosphorylation [17]. These findings highlight the inhibitory impact of MSCs on the TGF-β/Smad pathway. However, the precise underlying mechanisms remain elusive. Previous data showed that IL-10 and HGF exhibited renoprotective effects on injured kidneys. IL-10 exerts anti-fibrotic effects by inhibiting endoplasmic reticulum stress-mediated apoptosis [41]. In particular, HGF causes antifibrotic effects and prevents increases in myofibroblasts by blocking TGF-β signals [42]. In contrast, IDO and IGF have pro-fibrotic effects in DKD. IDO promotes renal tubular epithelial-mesenchymal transition and renal interstitial fibrosis by upregulating the expression of TGF-β1 [43, 44]. We found that MSCs can modulate the activation of the TGF-β signaling pathway through IL-10, HGF, IDO, and IGF-1, thereby influencing podocyte fibrosis. Immunohistochemical

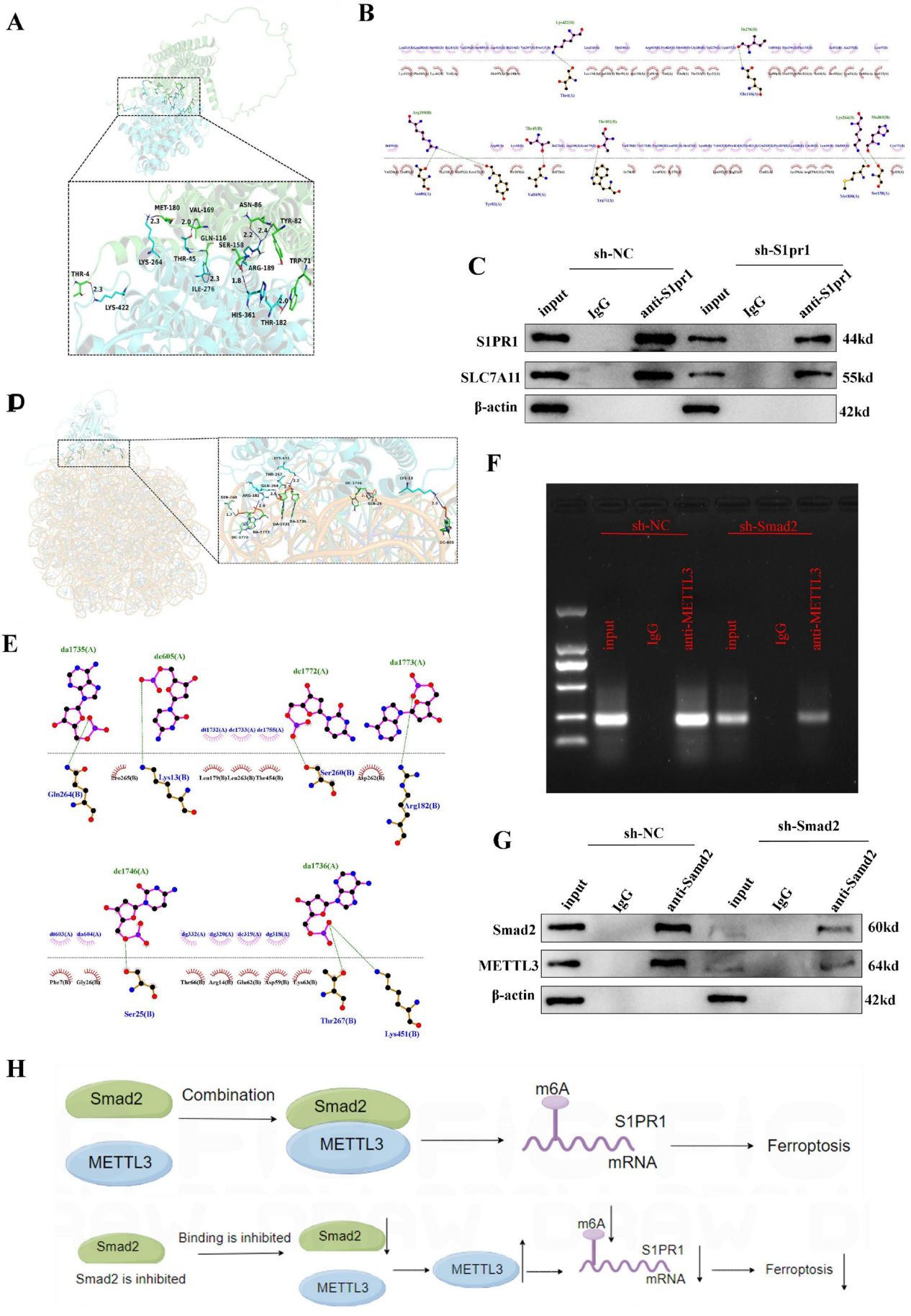

FIGURE 8 | Legend on next page.

FIGURE 8 | Functional Interactions and Regulatory Crosstalk Between Smad2, METTL3, S1PR1, and SLC7A11. (A) 3D model of the S1PR1-SLC7A11 complex generated by HDOCK. S1PR1 (A-chain, green) and SLC7A11 (B-chain, cyan) are shown in cartoon/sticks representation. (B) 2D model of the S1PR1-SLC7A11 complex generated by HDOCK. In the 2D visualization diagram, carbon atoms are represented by black circles, oxygen atoms by red circles, and nitrogen atoms by blue circles. Hydrophobic interactions are depicted as red and pink semicircles, while hydrogen bond interactions are shown as green dashed lines. (C) Co-IP assay was applied in MPC5 protein lysates using separately anti-S1PR1 or anti-IgG, and then, the levels of S1PR1 and SLC7A11 were detected by western blot. (D) The HDOCK tool was used to analyze the binding mode and docking score of the Smad2-S1PR1-mRNA complex, and a 3D visualization of the results was generated. The green cartoon/sticks represent S1PR1-mRNA (Chain A), the cyan cartoon/sticks represent the Smad2 protein (Chain B), and the blue dashed lines indicate hydrogen bond interactions. (E) The HDOCK tool was employed to analyze the binding mode and docking score of the Smad2-S1pr1-mRNA complex, with the results presented in a 2D diagram. In this diagram, carbon atoms are depicted as black circles, oxygen atoms as red circles, and nitrogen atoms as blue circles. Hydrophobic interactions are illustrated by red and pink semicircles, while hydrogen bond interactions are indicated by green dashed lines. (F) CHIP-PCR assays were performed with MPC5 cells. Chromatin fragments were pulled down with anti-METTL3, using IgG as a control. Semi-quantitative PCRs were performed using specific S1PR1 promoter primers. (G) Co-IP assay was applied in MPC5 protein lysates using separately anti-Smad2 or anti-IgG, and then, the levels of Smad2 and METTL3 were detected by western blot. (H) Schematic diagram. All in vitro experiments were performed with at least three independent replicates.

analysis of kidney tissues further revealed that MSC administration significantly reduced the expression of Smad2/3, including in podocytes. Podocyte injury or loss is widely regarded as a critical event in the progression of DKD, and therapeutic strategies targeting podocytes are expected to decelerate disease progression and lower the risk of developing ESRD [45]. MSCs have been reported to alleviate podocyte inflammation and injury, thereby improving renal function [46, 47].

In preliminary studies, transcriptome sequencing and bioinformatics analysis of high-glucose-induced HK-2 cells following MSC intervention enriched pathways and genes associated with ferroptosis (e.g., ACSL4, SLC3A2), indicating that ferroptosis may play a key role in the onset and progression of DKD. This finding prompted further investigation of ferroptosis in other renal intrinsic cells.

Our study demonstrated that podocytes undergo ferroptosis in a high-glucose environment, and MSC treatment effectively alleviated this process. Additionally, Smad2/3 has been revealed to interact with the methyltransferase complex, regulating transcription and m6A modifications of downstream molecules [20]. In DKD, increased m6A modifications were observed, predominantly driven by METTL3.

This study provides insights into the mechanistic network linking MSCs, Smad2/3, METTL3, and podocyte ferroptosis.

Following MSC intervention, the proliferation of podocytes exposed to high-glucose conditions was enhanced, while apoptosis levels were significantly reduced. These findings indicate that podocytes serve as critical target cells for MSC-mediated therapeutic effects in DKD.

Previous studies have demonstrated that MSCs can alleviate pathological damage in mesangial cells and renal tubular epithelial cells [48–50]. This study further confirms the protective effects of MSCs on podocytes, indicating that the therapeutic mechanisms of MSCs extend to multiple types of renal intrinsic cells. These findings expand the potential therapeutic targets of MSCs in DKD, providing broader opportunities for their clinical application in managing this condition.

Ferroptosis, an oxidative form of cell death triggered by small molecular substances, has been identified as a critical contributor to podocyte injury and the progression of DKD [51]. Inhibiting ferroptosis has been revealed to alleviate podocyte damage and slow DKD progression [52]. Studies have demonstrated the potential to protect podocytes and improve renal function by silencing key ferroptosis-associated proteins [29]. Additionally, natural compounds and pharmaceutical agents with ferroptosis-inhibitory properties offer promising therapeutic avenues for DKD management [13].

The present findings expand the understanding of how ferroptosis contributes to the onset and progression of DKD, paving the way for future research focused on developing targeted drugs or therapies that modulate the ferroptosis pathway.

Through transcriptome sequencing and m6A-seq correlation analysis, *S1PR1* was identified as a downstream target gene influenced by Smad2/3 and METTL3. The study confirmed that S1PR1 plays a key role in regulating ferroptosis in podocytes. S1PR1 is one of five receptors for sphingosine-1-phosphate (S1P), collectively known as S1PR1–S1PR5 [53]. The S1P/S1prs signaling pathway is involved in lymphocyte migration and has been widely studied in immune and inflammatory diseases [54].

Among the five receptors, S1PR1 exhibits high expression levels in kidney tissues; however, its specific role in kidney diseases remains unclear [55]. Previous research has shown that S1PR1 transactivation by LDL enhances connective tissue growth factor (CTGF) expression in mesangial cells [56] and facilitates the migration of Th17 cells from the gut to the kidneys, thereby exacerbating autoimmune renal disease [57]. These findings indicate a potential disease-promoting role for S1PR1 in kidney diseases.

However, the present study revealed that S1PR1 exerts protective effects in DKD podocytes. Experimental findings demonstrated that S1PR1 expression levels are inversely correlated with Smad2, METTL3, and m6A modification levels. This confirms that the regulation of S1PR1 by Smad2 and METTL3 occurs in an m6A-dependent manner.

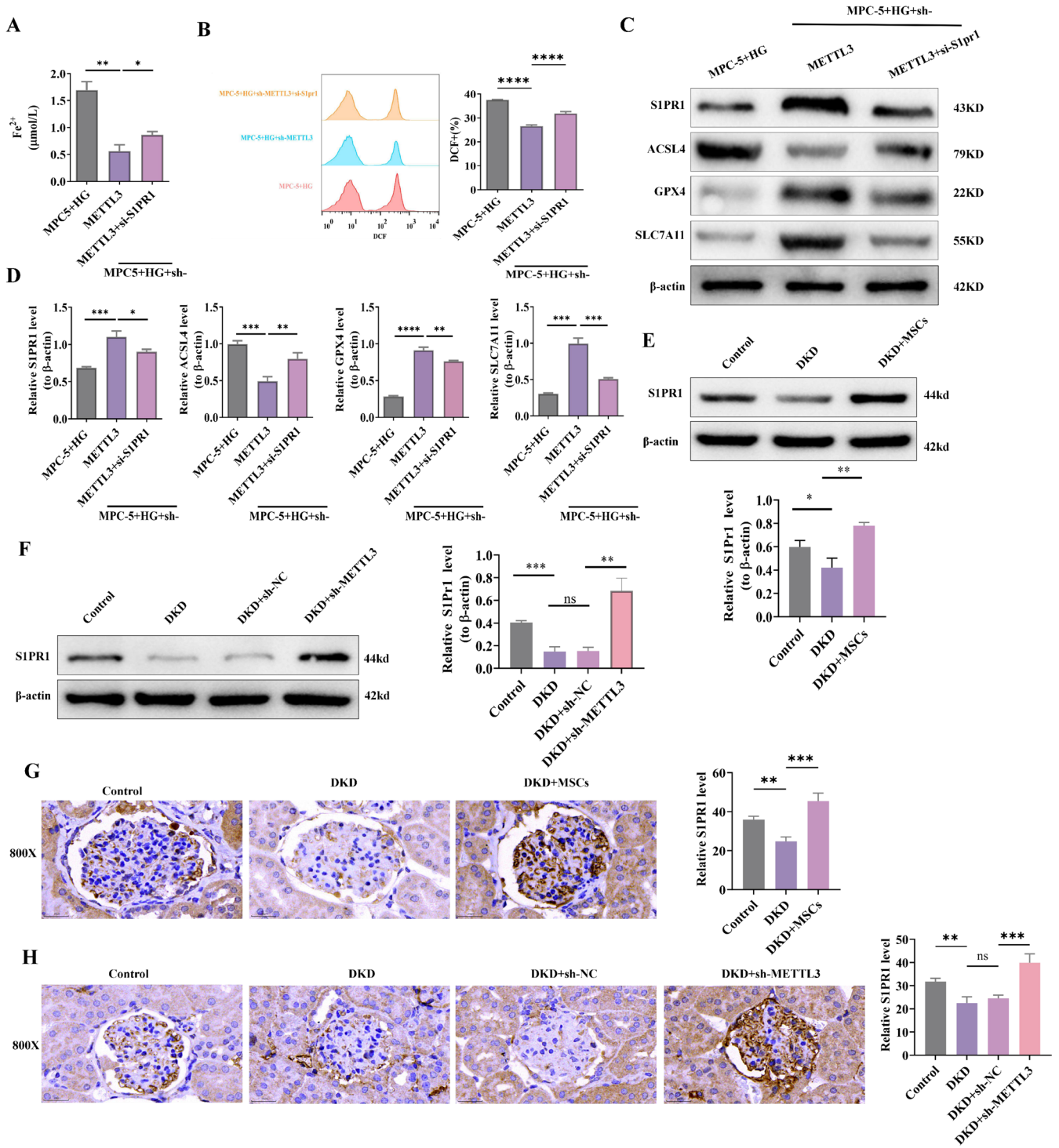

FIGURE 9 | Role of S1PR1 in regulating ferroptosis: (A) ELISA assay measuring Fe^{2+} content in MPC5 cells to assess ferroptosis activity. (B) Flow cytometry analysis of ROS levels in MPC5 cells, including flow cytometry plots and corresponding bar charts quantifying ROS content. (C, D) Western blot analysis detecting protein levels of S1PR1, ACSL4, GPX4, and SLC7A11 in MPC5 cells, with β-actin as the loading control. (E) Western blot analysis of S1PR1 protein expression, using β-Actin as the loading control. (F) Confirmation of S1PR1 protein expression levels through western blot analysis, with β-actin as the loading control. (G) Immunohistochemistry analysis of S1PR1 expression in kidney tissue. (H) Validation of S1PR1 expression in kidney tissue through additional immunohistochemistry analysis. Each group consisted of 6 mice, and all mice participated in and underwent all experimental assessments. All in vitro experiments were performed with at least three independent replicates (*$p < 0.05$; **$p < 0.01$; ***$p < 0.001$; ****$p < 0.0001$).

Consistent with these findings, previous studies have demonstrated that SEW2871, a selective S1PR1 agonist, alleviates high-glucose-induced podocyte injury while upregulating nephrin and podocin expression, further confirming the protective role of S1PR1 in podocytes [58]. Collectively, these observations highlight the significant role of S1PR1 in various kidney diseases.

Given the cell-specific nature of S1PR1, its effects may vary across different renal cell types. Notably, this study demonstrated that the methylation and expression levels of S1PR1 influence ferroptosis in podocytes. Suppression of S1PR1 expression significantly alleviated markers associated with ferroptosis within the cells. Although the exact relationship between S1PR1 and ferroptosis is not fully understood, previous research has indicated that S1PR1 may interact with the FoxO signaling pathway to regulate downstream signaling.

The FoxO signaling pathway has been shown to inhibit ferroptosis in disease models such as cerebral ischemia–reperfusion (CIR) injury and osteoarthritis (OA) [59, 60]. This crosstalk provides a potential explanation for the regulatory role of S1PR1 in ferroptosis.

Our study has revealed a potential protein–protein interaction between S1PR1 and SLC7A11. SLC7A11 serves as a pivotal "upstream regulator" in ferroptosis suppression. By modulating the cystine–cysteine–glutathione axis, it directly intervenes in the core process of lipid peroxidation. Through synergistic action with GPX4, SLC7A11 eliminates lipid peroxides, thereby maintaining cell membrane integrity and preventing ferroptosis [61, 62]. It is plausible that S1PR1 binds to SLC7A11, thereby influencing its stability and function. This finding may offer further insights into the regulatory mechanism of S1PR1 on ferroptosis.

Importantly, these findings indicate that targeting S1PR1 activity or expression may reduce podocyte injury and ferroptosis, providing a novel therapeutic avenue. Given the renal protective effects of S1PR1, the development of drugs or therapeutic strategies targeting this receptor holds significant promise.

The TGF-β/Smad signaling pathway is a well-established regulator of fibrosis in tissues and organs [63, 64]. Its upregulation has been implicated as a key mechanism in the progression of CKD [65]. Consistent with these findings, this study demonstrated increased levels of Smad2, Smad3, and their phosphorylated forms in both in vivo and in vitro DKD models, a phenomenon mitigated by MSC intervention [17].

Previous studies have reported that Smad2/3 interacts with the methyltransferase complex within the nucleus [20]. In this study, increased nuclear translocation of Smad2/3 was observed in podocytes from DKD models. Concurrently, high-glucose-induced MPC5 cells exhibited elevated expression of m6A methyltransferases (METTL3, METTL14, and WTAP) and reduced levels of demethylases (ALKBH5 and FTO). Importantly, METTL3 and ALKBH5 demonstrated strong diagnostic potential for DKD.

Given its role as a key catalytic subunit in the METTL3-METTL14-WTAP complex (MTC), METTL3 was selected for further investigation [66]. Knocking down METTL3 reversed the elevated m6A modification levels induced by Smad2 overexpression, supporting the hypothesis that Smad2 enhances m6A modifications via METTL3. These findings emphasize the importance of exploring the interplay between Smad signaling and m6A modifications in elucidating DKD pathogenesis.

5 | Conclusion

This study confirmed that Smad2 promotes m6A modification of the *S1PR1* gene by entering the nucleus and interacting with METTL3, thereby influencing S1PR1 expression and positively regulating cellular ferroptosis in DKD models. MSC intervention attenuated this process, providing further mechanistic insights into how MSCs alleviate DKD.

In conclusion, the findings establish that MSCs improve DKD by inhibiting ferroptosis through modulation of the Smad2/3/METTL3/S1PR1 axis.

Author Contributions

Yi-Hua Bai, Hong-Ying Jiang designed the research. Li-Lan Huang, Yue-Yuan Hou, Ji Yang, Xing-Na Liao, Jin-Sha Ma, Wen-Chao Wang, Yi-Xiao Quan collected data. Li-Lan Huang, Yue-Yuan Hou, Ji Yang, Xing-Na Liao, Yi-Hua Bai, Hong-Ying Jiang conducted data analysis. Li-Lan Huang, Jin-Sha Ma, Wen-Chao Wang, Yi-Xiao Quan, Yi-Hua Bai conducted statistical analysis. Yi-Hua Bai, Hong-Ying Jiang, Li-Lan Huang won the fund. Li-Lan Huang, Yi-Hua Bai wrote the manuscript. Li-Lan Huang, Yi-Hua Bai have made the final revisions to the manuscript.

Ethics Statement

All animal experiments were approved by the Institutional Animal Care and Use Committee at the Second Hospital Affiliated to Kunming Medical University (Ethics No.: Kmmu20211132), and were conducted in compliance with the Animal Research: Reporting of In Vivo Experiments (ARRIVE) guidelines.

Conflicts of Interest

The authors declare no conflicts of interest.

Data Availability Statement

The datasets generated and/or analyzed during the current study are not publicly available but are available from the corresponding author (Yi-Hua Bai) on reasonable request.

References

1. Y. Li, Y. Liu, S. Liu, et al., "Diabetic Vascular Diseases: Molecular Mechanisms and Therapeutic Strategies," *Signal Transduction and Targeted Therapy* 8, no. 1 (2023): 152.

2. K. Shahzad, S. Fatima, H. Khawaja, et al., "Podocyte-Specific Nlrp3 Inflammasome Activation Promotes Diabetic Kidney Disease," *Kidney International* 102, no. 4 (2022): 766–779.

3. F. Barutta, S. Bellini, S. Kimura, et al., "Protective Effect of the Tunneling Nanotube-TNFAIP2/M-Sec System on Podocyte Autophagy in Diabetic Nephropathy," *Autophagy* 19, no. 2 (2023): 505–524.

4. C. Zhao, Z. Pu, J. Gao, et al., "Multiomics Analyses Combined With Systems Pharmacology Reveal the Renoprotection of Mangiferin Monosodium Salt in Rats With Diabetic Nephropathy: Focus on Improvements in Renal Ferroptosis, Renal Inflammation, and Podocyte Insulin Resistance," *Journal of Agricultural and Food Chemistry* 71, no. 1 (2023): 358–381.

5. S. Assady, T. Benzing, M. Kretzler, and K. L. Skorecki, "Glomerular Podocytes in Kidney Health and Disease," *Lancet* 393, no. 10174 (2019): 856–858.

6. M. Ak and N. Sb, "KDOQI Commentary on the KDIGO 2022 Update to the Clinical Practice Guideline for Diabetes Management in CKD," *American Journal of Kidney Diseases* 83, no. 3 (2024): 277–287, https://pubmed.ncbi.nlm.nih.gov/38142396/.

7. American Diabetes Association Professional Practice Committee, "11. Chronic Kidney Disease and Risk Management: Standards of Care in Diabetes-2024," *Diabetes Care* 47, no. Suppl 1 (2024): S219–S230.

8. L. J. Hickson, A. Eirin, S. M. Conley, et al., "Diabetic Kidney Disease Alters the Transcriptome and Function of Human Adipose-Derived Mesenchymal Stromal Cells but Maintains Immunomodulatory and Paracrine Activities Important for Renal Repair," *Diabetes* 70, no. 7 (2021): 1561–1574.

9. Y. Huang and L. Yang, "Mesenchymal Stem Cells and Extracellular Vesicles in Therapy Against Kidney Diseases," *Stem Cell Research & Therapy* 12, no. 1 (2021): 219.

10. B. Lu and L. O. Lerman, "MSC Therapy for Diabetic Kidney Disease and Nephrotic Syndrome," *Nature Reviews. Nephrology* 19, no. 12 (2023): 754–755.

11. H. Wang, D. Liu, B. Zheng, et al., "Emerging Role of Ferroptosis in Diabetic Kidney Disease: Molecular Mechanisms and Therapeutic Opportunities," *International Journal of Biological Sciences* 19, no. 9 (2023): 2678–2694.

12. C. Yang, "Research Progress on Multiple Cell Death Pathways of Podocytes in Diabetic Kidney Disease," *Molecular Medicine* 29 (2023): 135.

13. J. Chen, Z. Ou, T. Gao, et al., "Ginkgolide B Alleviates Oxidative Stress and Ferroptosis by Inhibiting GPX4 Ubiquitination to Improve Diabetic Nephropathy," *Biomedicine & Pharmacotherapy* 156 (2022): 113953.

14. N. R. Gough, X. Xiang, and L. Mishra, "TGF-β Signaling in Liver, Pancreas, and Gastrointestinal Diseases and Cancer," *Gastroenterology* 161, no. 2 (2021): 434–452.e15.

15. Q. Hong, H. Cai, L. Zhang, et al., "Modulation of Transforming Growth Factor-β-Induced Kidney Fibrosis by Leucine-Rich α-2 Glycoprotein-1," *Kidney International* 101, no. 2 (2022): 299–314.

16. Y. Bai, J. Wang, Z. He, M. Yang, L. Li, and H. Jiang, "Mesenchymal Stem Cells Reverse Diabetic Nephropathy Disease via Lipoxin A4 by Targeting Transforming Growth Factor β (TGF-β)/Smad Pathway and Pro-Inflammatory Cytokines," *Medical Science Monitor* 25 (2019): 3069–3076.

17. Y. Bai, L. Huang, Y. Fan, and Y. Li, "Marrow Mesenchymal Stem Cell Mediates Diabetic Nephropathy Progression via Modulation of Smad2/3/WTAP/m6A/ENO1 Axis," *FASEB Journal* 38 (2024): e23729.

18. S. Song, C. Shi, Y. Bian, et al., "Sestrin2 Remedies Podocyte Injury via Orchestrating TSP-1/TGF-β1/Smad3 Axis in Diabetic Kidney Disease," *Cell Death & Disease* 13, no. 7 (2022): 663.

19. C. Qi, Y. Hu, M. Zeng, et al., "Verteporfin Inhibits the Dedifferentiation of Tubular Epithelial Cells via TGF-β1/Smad Pathway but Induces Podocyte Loss in Diabetic Nephropathy," *Life Sciences* 311, no. Pt B (2022): 121186.

20. A. Bertero, S. Brown, P. Madrigal, et al., "The SMAD2/3 Interactome Reveals That TGFβ Controls m6A mRNA Methylation in Pluripotency," *Nature* 555, no. 7695 (2018): 256–259.

21. X. Deng, Y. Qing, D. Horne, H. Huang, and J. Chen, "The Roles and Implications of RNA m6A Modification in Cancer," *Nature Reviews. Clinical Oncology* 20, no. 8 (2023): 507–526.

22. J. Liu, X. Dou, C. Chen, et al., "N^6-Methyladenosine of Chromosome-Associated Regulatory RNA Regulates Chromatin State and Transcription," *Science* 367, no. 6477 (2020): 580–586.

23. R. Bechara, N. Amatya, R. D. Bailey, et al., "The m6A Reader IMP2 Directs Autoimmune Inflammation Through an IL-17- and TNFα-Dependent C/EBP Transcription Factor Axis," *Science Immunology* 6, no. 61 (2021): eabd1287.

24. K. W. Jia, R. Q. Yao, Y. W. Fan, et al., "Interferon-α Stimulates DExH-Box Helicase 58 to Prevent Hepatocyte Ferroptosis," *Military Medical Research* 11, no. 1 (2024): 22.

25. W. Wu, Y. Jin, L. Teng, et al., "Mitochondria-Related Reversal of Early-Stage Diabetic Nephropathy in Donor Kidney After Transplantation in Mice," *Annals of Translational Medicine* 7, no. 24 (2019): 801.

26. W. Wang, M. Green, J. E. Choi, et al., "$CD8^+$ T Cells Regulate Tumour Ferroptosis During Cancer Immunotherapy," *Nature* 569, no. 7755 (2019): 270–274.

27. K. Ding, C. Liu, L. Li, et al., "Acyl-CoA Synthase ACSL4: An Essential Target in Ferroptosis and Fatty Acid Metabolism," *Chinese Medical Journal* 136, no. 21 (2023): 2521–2537, https://doi.org/10.1097/CM9.0000000000002533.

28. H. Ma, X. Chen, S. Mo, et al., "Targeting N-Glycosylation of 4F2hc Mediated by Glycosyltransferase B3GNT3 Sensitizes Ferroptosis of Pancreatic Ductal Adenocarcinoma," *Cell Death and Differentiation* 30, no. 8 (2023): 1988–2004.

29. W. Y. Wu, Z. X. Wang, T. S. Li, et al., "SSBP1 Drives High Fructose-Induced Glomerular Podocyte Ferroptosis via Activating DNA-PK/p53 Pathway," *Redox Biology* 52 (2022): 102303.

30. W. Liu, Z. Xiong, T. Fu, et al., "Regulation of Renal Ischemia-Reperfusion Injury and Tubular Epithelial Cell Ferroptosis by PPARγ m6a Methylation: Mechanisms and Therapeutic Implications," *Biology Direct* 19, no. 1 (2024): 99.

31. L. Liu, "Insights Into N6-Methyladenosine and Programmed Cell Death in Cancer," *Molecular Cancer* 21 (2022): 32.

32. X. Bao, Y. Zhang, H. Li, et al., "RM2Target: A Comprehensive Database for Targets of Writers, Erasers and Readers of RNA Modifications," *Nucleic Acids Research* 51, no. D1 (2023): D269–D279.

33. H. Tamiya, Y. Tamura, S. Mochi, et al., "Extended Sedentary Time Increases the Risk of All-Cause Death and New Cardiovascular Events in Patients With Diabetic Kidney Disease," *Circulation Journal* 84, no. 12 (2020): 2190–2197.

34. D. J. Magliano, E. J. Boyko, and IDF Diabetes Atlas 10th edition scientific committee, *IDF DIABETES ATLAS [Internet]*, 10th ed. (International Diabetes Federation, 2021), http://www.ncbi.nlm.nih.gov/books/NBK581934/.

35. C. Sávio-Silva, P. E. Soinski-Sousa, A. Simplício-Filho, R. M. C. Bastos, S. Beyerstedt, and É. B. Rangel, "Therapeutic Potential of Mesenchymal Stem Cells in a Pre-Clinical Model of Diabetic Kidney Disease and Obesity," *International Journal of Molecular Sciences* 22 (2021): 1546.

36. D. M. Hoang, "Stem Cell-Based Therapy for Human Diseases," *Signal Transduction and Targeted Therapy* 7 (2022): 272.

37. F. Zhou, "Biological Characteristics of Umbilical Cord Mesenchymal Stem Cells and Its Therapeutic Potential for Hematological Disorders," *Frontiers in Cell and Developmental Biology* 9 (2021): 570179.

38. C. Mennan, K. Wright, A. Bhattacharjee, B. Balain, J. Richardson, and S. Roberts, "Isolation and Characterisation of Mesenchymal Stem Cells From Different Regions of the Human Umbilical Cord," *BioMed Research International* 2013 (2013): 916136.

39. H. J. Park, "A Non-Biodegradable Scaffold-Free Cell Sheet of Genome-Engineered Mesenchymal Stem Cells Inhibits Development of Acute Kidney Injury," *Kidney International* 99 (2021): 117–133.

40. J. Y. Cao, B. Wang, T. T. Tang, et al., "Exosomal miR-125b-5p Deriving From Mesenchymal Stem Cells Promotes Tubular Repair by Suppression of p53 in Ischemic Acute Kidney Injury," *Theranostics* 11, no. 11 (2021): 5248–5266.

41. K. Jung, T. Lee, J. Kim, E. Sung, and I. Song, "Interleukin-10 Protects Against Ureteral Obstruction-Induced Kidney Fibrosis by Suppressing

Endoplasmic Reticulum Stress and Apoptosis," *International Journal of Molecular Sciences* 23, no. 18 (2022): 10702.

42. J. Yang and Y. Liu, "Blockage of Tubular Epithelial to Myofibroblast Transition by Hepatocyte Growth Factor Prevents Renal Interstitial Fibrosis," *Journal of the American Society of Nephrology* 13, no. 1 (2002): 96–107.

43. L. H. G. Matheus, G. M. Simão, T. A. Amaral, et al., "Indoleamine 2, 3-Dioxygenase (IDO) Increases During Renal Fibrogenesis and Its Inhibition Potentiates TGF-β 1-Induced Epithelial to Mesenchymal Transition," *BMC Nephrology* 18, no. 1 (2017): 287.

44. R. Dong, J. Yu, F. Yu, S. Yang, Q. Qian, and Y. Zha, "IGF-1/IGF-1R Blockade Ameliorates Diabetic Kidney Disease Through Normalizing Snail1 Expression in a Mouse Model," *American Journal of Physiology—Endocrinology and Metabolism* 317, no. 4 (2019): E686–E698.

45. S. Mohandes, T. Doke, H. Hu, D. Mukhi, P. Dhillon, and K. Susztak, "Molecular Pathways That Drive Diabetic Kidney Disease," *Journal of Clinical Investigation* 133, no. 4 (2023): e165654.

46. W. Yang, L. Chen, Y. Jhuang, et al., "Injection of Hybrid 3D Spheroids Composed of Podocytes, Mesenchymal Stem Cells, and Vascular Endothelial Cells Into the Renal Cortex Improves Kidney Function and Replenishes Glomerular Podocytes," *Bioengineering & Translational Medicine* 6, no. 2 (2021): e10212.

47. L. Peng, Y. Chen, S. Shi, and H. Wen, "Stem Cell-Derived and Circulating Exosomal microRNAs as New Potential Tools for Diabetic Nephropathy Management," *Stem Cell Research & Therapy* 13, no. 1 (2022): 25.

48. C. Ji, J. Zhang, H. Shi, et al., "Single-Cell RNA Transcriptomic Reveal the Mechanism of MSC Derived Small Extracellular Vesicles Against DKD Fibrosis," *Journal of Nanobiotechnology* 22, no. 1 (2024): 339.

49. W. Chen, F. Zhang, X. Hou, H. Xu, and D. Tang, "Ameliorating Role of microRNA-378 Carried by Umbilical Cord Mesenchymal Stem Cells-Released Extracellular Vesicles in Mesangial Proliferative Glomerulonephritis," *Cell Communication and Signaling: CCS* 20, no. 1 (2022): 28.

50. Q. Guo, J. Chen, J. Wu, et al., "Bioprinted Mesenchymal Stem Cell Microfiber-Derived Extracellular Vesicles Alleviate Unilateral Renal Ischemia-Reperfusion Injury and Fibrosis by Inhibiting Tubular Epithelial Cells Ferroptosis," *Bioactive Materials* 40 (2024): 649–664.

51. X. Jiang, B. R. Stockwell, and M. Conrad, "Ferroptosis: Mechanisms, Biology, and Role in Disease," *Nature Reviews Molecular Cell Biology* 22 (2021): 266–282.

52. Q. Zhang, Y. Hu, J. E. Hu, et al., "Sp1-Mediated Upregulation of Prdx6 Expression Prevents Podocyte Injury in Diabetic Nephropathy via Mitigation of Oxidative Stress and Ferroptosis," *Life Sciences* 278 (2021): 119529.

53. T. Derfuss, M. Mehling, A. Papadopoulou, A. Bar-Or, J. A. Cohen, and L. Kappos, "Advances in Oral Immunomodulating Therapies in Relapsing Multiple Sclerosis," *Lancet Neurology* 19, no. 4 (2020): 336–347.

54. M. P. McGinley and J. A. Cohen, "Sphingosine 1-Phosphate Receptor Modulators in Multiple Sclerosis and Other Conditions," *Lancet* 398, no. 10306 (2021): 1184–1194.

55. Y. Drexler, J. Molina, A. Mitrofanova, A. Fornoni, and S. Merscher, "Sphingosine-1-Phosphate Metabolism and Signaling in Kidney Diseases," *Journal of the American Society of Nephrology* 32, no. 1 (2021): 9–31.

56. H. M. El-Shewy, M. Sohn, P. Wilson, et al., "Low-Density Lipoprotein Induced Expression of Connective Tissue Growth Factor via Transactivation of Sphingosine 1-Phosphate Receptors in Mesangial Cells," *Molecular Endocrinology* 26 (2012): 833–845.

57. C. F. Krebs, H. J. Paust, S. Krohn, et al., "Autoimmune Renal Disease Is Exacerbated by S1P-Receptor-1-Dependent Intestinal Th17 Cell Migration to the Kidney," *Immunity* 45, no. 5 (2016): 1078–1092.

58. A. S. Awad, M. D. Rouse, K. Khutsishvili, et al., "Chronic Sphingosine 1-Phosphate 1 Receptor Activation Attenuates Early-Stage Diabetic Nephropathy Independent of Lymphocytes," *Kidney International* 79, no. 10 (2012): 1090–1098.

59. M. S. Mutabaruka, M. Pata, and J. Vacher, "A Foxo1-Klf2-S1pr1-Gnai1-Rac1 Signaling Axis Is a Critical Mediator of Ostm1 Regulatory Network in T Lymphopoiesis," *iScience* 25, no. 4 (2022): 104160.

60. J. P. Weber, F. Fuhrmann, R. K. Feist, et al., "ICOS Maintains the T Follicular Helper Cell Phenotype by Down-Regulating Krüppel-Like Factor 2," *Journal of Experimental Medicine* 212, no. 2 (2015): 217–233.

61. J. Xiao, C. Luo, A. Li, et al., "Icariin Inhibits Chondrocyte Ferroptosis and Alleviates Osteoarthritis by Enhancing the SLC7A11/GPX4 Signaling," *International Immunopharmacology* 133 (2024): 112010.

62. E. Mishima, T. Nakamura, S. Doll, et al., "Recommendations for Robust and Reproducible Research on Ferroptosis," *Nature Reviews. Molecular Cell Biology* (2025): 1471.

63. J. H. Lee and J. Massagué, "TGF-β in Developmental and Fibrogenic EMTs," *Seminars in Cancer Biology* 86 (2022): 136–145.

64. R. Diwan, H. N. Bhatt, E. Beaven, and M. Nurunnabi, "Emerging Delivery Approaches for Targeted Pulmonary Fibrosis Treatment," *Advanced Drug Delivery Reviews* 204 (2024): 115147.

65. Y. Shi, M. Tao, H. Chen, et al., "Ubiquitin-Specific Protease 11 Promotes Partial Epithelial-To-Mesenchymal Transition by Deubiquitinating the Epidermal Growth Factor Receptor During Kidney Fibrosis," *Kidney International* 103, no. 3 (2023): 544–564.

66. D. Han, A. P. Longhini, X. Zhang, V. Hoang, M. Z. Wilson, and K. S. Kosik, "Dynamic Assembly of the mRNA m6A Methyltransferase Complex Is Regulated by METTL3 Phase Separation. Gilbert WV, Editor," *PLoS Biology* 20, no. 2 (2022): e3001535.

Supporting Information

Additional supporting information can be found online in the Supporting Information section.